The scientist has a lot of experience with ignorance and doubt and uncertainty, and this experience is of very great importance, I think. When a scientist doesn't know the answer to a problem, he is ignorant. When he has a hunch as to what the result is, he is uncertain. And when he is pretty damn sure of what the result is going to be, he is still in some doubt. We have found it of paramount importance that in order to progress, we must recognize our ignorance and leave room for doubt. Scientific knowledge is a body of statements of varying degrees of certainty - some most unsure, some nearly sure, but none absolutely certain. Now, we scientists are used to this, and we take it for granted that it is perfectly consistent to be unsure, that it is possible to live and not know. But I don't know whether everyone realizes this is true. Our freedom to doubt was born out of a struggle against authority in the early days of science. It was a very deep and strong struggle: permit us to question - to doubt - to not be sure. I think that it is important that we do not forget this struggle and thus perhaps lose what we have gained.

Richard Feynman

I may be a minority of one in advocating that one should NOT separate science and politics - partly because I am old enough to remember the Weimar Republic before 1934...

Edwin Ernest Salpeter

Contents

Sommario

Questa tesi si propone di studiare, tramite l'ausilio di simulazioni idrodinamiche, l'interazione tra getti generati dal buco nero supermassivo al centro delle galassie ellittiche (in particolare quelle molto massive) e il gas caldo circostante.

Questo studio risulta interessante nell'ambito del cosiddetto "cooling flow problem", tipico anche di strutture più grandi come gruppi e ammassi di galassie; difatti, in tutte queste strutture, ci si aspetta che il gas collassi lentamente in una situazione di quasi-equilibrio, raggiungendo la temperatura viriale. Ciò fa sì, però, che il tempo di raffreddamento del gas al centro della galassia sia inferiore al "tempo di vita" del sistema e che esso, quindi, raffreddi rapidamente, irradiando in banda X, in un tempo scala tipico di $\sim 10^7 - 10^8$ anni. Questo fenomeno dovrebbe dar luogo ad un picco di luminosità e a temperature centrali molto basse, ma, dalle osservazioni, l'entità del raffreddamento risulta essere inferiore, almeno di un ordine di grandezza, rispetto al classico modello di cooling flow a cui si è accennato. Per spiegare tale comportamento, tutt'ora si invoca anche, non senza ulteriori questioni aperte, la possibilità che questo gas a basse temperature non sia osservato.

Negli anni si è tuttavia trovata una buona soluzione nella presenza di un feedback dovuto ad accrescimento sul buco nero supermassivo centrale, sia esso nella fase di AGN o in una fase semi-quiescente a tassi di accrescimento notevolmente minori. Questa ipotesi è effettivamente sempre più corroborata da evidenze osservative, come, ad esempio, emissione radio bipolare osservata in molte galassie ellittiche, valori elevati dell'entropia centrale oppure, tramite recenti osservazioni con i satelliti XMM e Chandra, evidenti perturbazioni non isotrope osservate nel gas, in forma di cavità e shock. Uno dei casi più tipici in questo senso, su scala galattica, è sicuramente quello di NGC 4636 che ha mostrato diverse strutture "anomale", evidenti in differenti osservazioni in banda X, in particolare due "bracci" luminosi e simmetrici che si dipartono dal

centro galattico (vedi Jones et al., 2002; O'Sullivan et al., 2005; Baldi et al., 2009).

È sembrato particolarmente interessante, di conseguenza, verificare se fosse possibile riprodurre queste strutture attraverso simulazioni idrodinamiche effettuate, in coordinate cilindriche, con un codice euleriano bidimensionale basato su ZEUS-2D (Stone and Norman, 1992).

A bassa risoluzione è stato dapprima simulato un cooling flow classico e poi si è cercato di introdurre l'effetto di un getto, utilizzando 2 approcci ricorrenti in letteratura. Il primo consiste nel simulare getti massivi sub-relativistici, con trasporto di momento ed energia (vedi, ad esempio, Basson and Alexander, 2003; Omma et al., 2004; Brighenti and Mathews, 2006; Sternberg and Soker, 2009; Gaspari et al., 2011), assegnando densità e velocità tipici ad una regione cilindrica nell'origine degli assi. Il secondo consiste nel simulare artificialmente una cavità generata dalla testa di un getto relativistico (vedi, ad esempio, Brüggen and Kaiser, 2002; Mathews and Brighenti, 2008; Brüggen and Scannapieco, 2009): si è perciò fissato un input di energia ad una certa distanza dal centro galattico. Il minor costo computazionale della bassa risoluzione è servito per discriminare i valori ottimali dei parametri in gioco. Si è scoperto che entrambi i modelli falliscono nel riprodurre con esattezza tutte le caratteristiche osservate da Baldi et al. (2009).

Ad alta risoluzione si è perciò deciso di privilegiare il modello di getto massivo, più efficace nel confronto con le osservazioni e in quanto capace di descrivere l'evoluzione idrodinamica del feedback in maniera più completa e realistica. Si è perciò simulato un Best model, effettuando anche uno studio sull'evoluzione della metallicità in presenza di un getto.

Si è infine passati, a latere, seppur in maniera parziale, ad indagare il comportamento del getto a seguito di una grande variazione dei parametri. Si è scoperto, in particolare, che i parametri densità e velocità sembrano avere influenza, in maniera indipendente, sulla struttura generale del getto e che la turbolenza generata dall'instabilità di Kelvin-Helmoltz può avere un ruolo importante nel sottrarre energia cinetica al getto.

Abstract

The aim of this thesis is to study, through hydrodynamical simulations, the interaction between jets from the supermassive black hole at the center of elliptical galaxies (particularly the most massive ones) and the ambient hot gas emitting in the X band.

This study results particularly interesting with respect to the "cooling flow problem", also typical of other scales like those of groups and clusters of galaxies; in fact, in all these structures, we should expect the gas to have a slowly collapse in quasi-equilibrium, reaching the virial temperature. In this case, the central gas is expect to rapidly cool in a typical timescale of $\sim 10^7 - 10^8$ year, since its cooling time becomes lower than the age of the system. This phenomenon should lead to a central peak in the X-ray luminosity and low central temperatures, but the observations show that the cooling is less than that expected from the mentioned classical cooling flow model, at least of an order of magnitudine. The possibility that is gas is somehow hidden is nowaday still invoked, even if this explanation leads to other unsolved questions.

Throughout the years a good solution has been found in the presence of a feedback due to accretion onto the central supermassive black hole, either in AGN phase or in a semi-quiescent phase at lower accretion rates. This hypotesis is effectively more and more supported by observational evidencies, like, for example, bipolar radio emission observed in many elliptical galaxies, high entropy values in the center of these systems or the presence of evident unisotropic disturbancies in the hot gas, like cavities and shocks, recently observed by XMM and Chandra satellites. One of the most typical examples of such disturbancies on the galactic scale is that of NGC 4636 which shows many "anomalous" features in its X-ray image and, in particular, two bright and symmetric "arm-like" structures departing from the galactic center (see Jones et al., 2002; O'Sullivan et al., 2005; Baldi et al., 2009).

It seemed, consequently, interesting to try to reproduce such structures through hydrodynamical simulations in cylindrical coordinates performed with a eulerian two-dimensional code based on ZEUS-2D (Stone and Norman, 1992).

At low resolution I first simulated a classical cooling flow and then I tried to model the effect of a jet, adopting two different approaches frequently used in literature. The first one consists in simulating mass-loaded subrelativistic jets, with transfer of energy and momentum (see, for example, Basson and Alexander, 2003; Omma et al., 2004; Brighenti and Mathews, 2006; Sternberg and Soker, 2009; Gaspari et al., 2011), setting typical density and velocity in a cylindrical region at the origin of the axes. The second one consists in simulating an “artificial” cavity created and fed by the head of a relativistic jet (see, for example, Brüggen and Kaiser, 2002; Mathews and Brighenti, 2008; Brüggen and Scannapieco, 2009): in this case I fixed a energy input at a certain distance from the galactic center. The low computational cost of low resolution runs has been useful to seek and find the best values of the characteristic parameters.

The second step consisted in simulating at high resolution the Best model found, also trying to trace the evolution of iron abundance with the presence of a jet.

Finally, a latere, I tested the general behaviour of mass-loaded jets, though with a partial and not exhaustive approach, trying to understand how the density and velocity, after a huge variation of these parameters, can affect and change the global structure of the jet.

The thesis is so structured: in Chapter 1 I will describe the properties of the hot gas in elliptical galaxies, in Chapter 2 I will introduce the “cooling problem”, describing its possible solutions, in Chapter 3 I will present the most recent observation in X band of NGC 4636 by Baldi et al. (2009), while in Chapters 4 and 5 I will show the results of my work. A brief description of the used hydrodynamical code can be found in the Appendix.

Chapter 1

The X-ray hot gas in elliptical galaxies

Before the first Einstein X-ray observations of elliptical galaxies (for example, Forman et al., 1985; Canizares et al., 1987; Fabbiano et al., 1992), they were believed to be gas free, with the gas from stellar mass loss being removed by winds driven by Type Ia supernovae. However the Einstein observations showed extended hot gas halos surrounding the optical extension of elliptical galaxies (see Fig. 1.1). Following observations carried out in the '90s with the Röntgensatellite (ROSAT) allowed extensive galaxy surveys , detecting X-ray emission from hundred of galaxies (e.g., O'Sullivan et al., 2001). In the later years, XMM-Newton (ESA) and Chandra (NASA) satellites opened a new era in the understanding of the hydrodynamic histories of galaxies and clusters (for example, Sansom et al., 2006; Diehl and Statler, 2007; Jones et al., 2002).

The hot gas in and around elliptical galaxies is of particular interest, because its origin and metal enrichment are closely linked with the merger origin of elliptical galaxies in groups and clusters: a better understanding of its properties can provide clues as to the structure formation scenario. It also gives us important informations about the stellar kinematics and mass-to-light ratios (Fukazawa et al., 2006; Gastaldello et al., 2007; Brighenti and Mathews, 1997).

The evolution and physical condition of the hot gas in rich clusters of galaxies and in individual elliptical galaxies are similar in many ways, but there are some important distinctions that makes the latter even more appealing in some cases. For example, as explained by Mathews and Brighenti (2003a), in a hierarchical structure formation scenario, smaller structures are often older, so the hot gas in elliptical galaxies and their associated galaxy groups is expected to be less disturbed by ongoing mergers than their younger, more massive cluster counterparts. In X-ray bright E galaxies that are rather isolated (and likely undisturbed), the metallicity gradient can give a unique information about star and galaxy formation in the distant past. This vital information is lost when such groups merge and mix to form rich clusters. Another key attribute of hot gas on galactic scales is the likely importance of stellar mass loss and continued Type Ia supernova activity in supplying and enriching the hot gas. Finally, the properties of the hot gas can be determined with more confidence on galactic scales, where the gravitational potential is better known from the stellar light distribution.

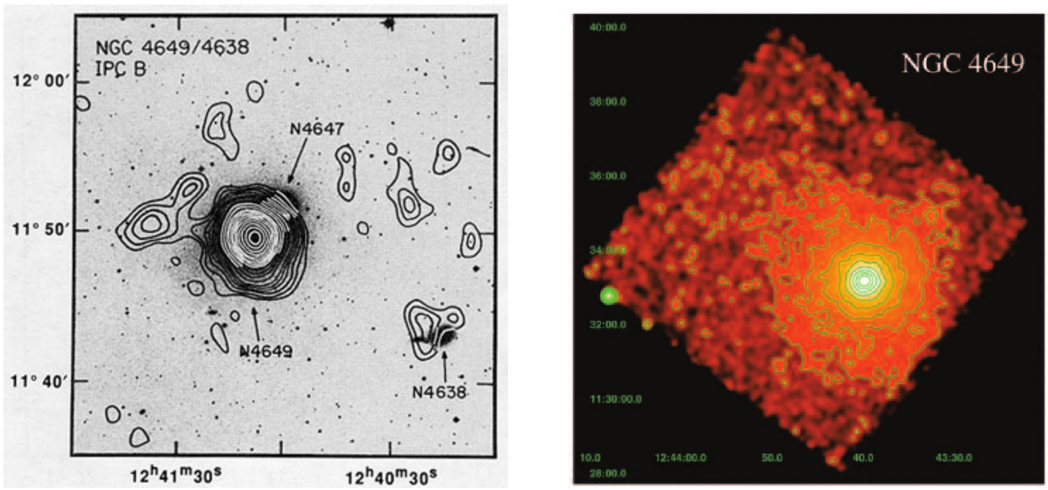

Figure 1.1: Left: Einstein IPC B X-ray emission contour map of NGC 4649 overlaid on the optical image from Fabbiano et al. (1992). Right: Chandra X-ray image of NGC 4649 from Humphrey et al. (2006).

1.1 The origin of the X-ray hot gas

There are optical evidencies that elliptical galaxies formed at high redshift ($z \gtrsim 2$) and many theoretical works suggest that they formed by mergers in group environment (Merritt, 1985; Dubinski, 1998), before the formation of more massive galaxy clusters. It is almost obvious that the diffuse thermal gas in groups and clusters, which are "dynamically" hot, is also hot (Mathews and Brighenti, 2003a).

Hot gas in elliptical galaxies can have both an internal and an external origin. Concerning the internal origin, the continuous ejecta from evolving stars inside the galaxy occurs at a rate of $\sim 1.3[L_B/(10^{11} L_{B,\odot})] M_\odot \ yr^{-1}$

(Mathews and Brighenti, 2003a). This gas from orbiting red giant stars is then thermalized by shocks, reaching the stellar kinematic temperature $T_* \approx T_{vir} \approx \mu m_p \sigma^2/k_b \sim 1\ keV$, where μ is the mean atomic weight, m_p is the atomic mass of hydrogen, k_b is the Boltzmann's constant and σ is the stellar velocity dispersion. Also supernovae provide some additional heating. Type Ia supernovae are more effective at later evolutionary times, while, at early times, when most of galactic stars were forming, type II supernovae were frequent enough to drive winds of enriched gas into the local environment (Mathews and Brighenti, 2003a). Accretion from the ambient cosmological flow that is gravitationally bound to the surrounding group or cluster is an external source of gas. As external gas arrives after having fallen into the deeper potential well of the group/cluster, it is shock-heated to the virial temperature of the galaxy (Gunn and Gott, 1972; Bertschinger, 1985; Birnboim and Dekel, 2003). This phenomenon is successful in explaining many hot gas properties, most of all the increasing of gas temperature at great radii (Thomas, 1986; Bertin and Toniazzo, 1995; Brighenti and Mathews, 1998, 1999; Diehl and Statler, 2008b).

1.2 The properties of the hot gas: what is it teaching us?

1.2.1 General properties

X-ray surface brightness profiles of the hot gas X-ray emission are often analitycally well approximated by the isothermal β-model (Sarazin, 1986):

$$I_X(r) \propto (1 + (r/r_c))^{-3\beta+1/2}, \tag{1.1}$$

where r_c is the galaxy core radius and β is the ratio of the specific energy in stars to the specific energy in the hot gas

$$\beta \equiv \frac{\mu m_H {\sigma_r}^2}{k_b T_{gas}}.$$

Thus, the respective density profiles for the hot gas are described by

$$\rho_g(r) \propto (1 + (r/r_c))^{-3\beta/2}, \tag{1.2}$$

that matches the density profile for the King singular isothermal sphere (SIS), in the case $\beta = 1$. This is a simple parametrization and observations often

show more peaked density profile near the center of the galaxy. In these cases often a double $\beta - model$ is used.
The temperature profiles always show a positive dT/dr at little radii. The reason is that the gas, collapsing in the potential well of the galaxy, reaches, in the central region, a cooling time (see Eq. 2) that is shorter than the age of the system and cools in $10^7 - 10^8$ yr. We will better treat this topic in Chapter 2.
Fig. 1.2, from Humphrey et al. (2006), shows deprojected density and temperature profiles for NGC 4472.

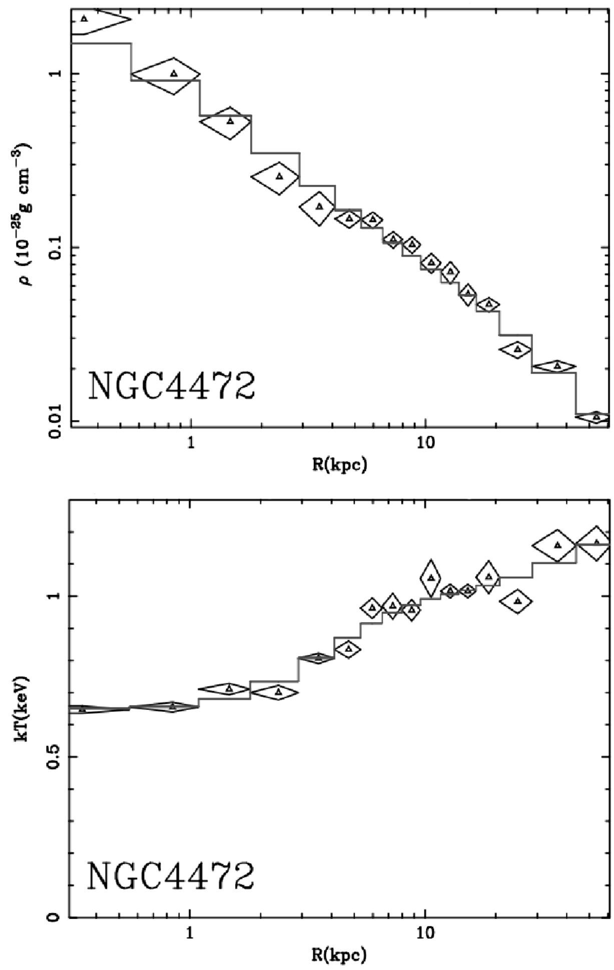

Figure 1.2: Deprojected density and temperature profiles of the X-ray hot gas for NGC 4472 from Humphrey et al. (2006).

1.2.2 The fundamental plane

Elliptical galaxies are often described by three main observational parameters: the central stellar velocity dispersion σ_0, the half-light "effective" radius R_e and the mean "effective" surface brightness Σ_e.
It has been observed that elliptical galaxies populate a narrow plane, the well-known "fundamental plane", in this three-dimensional parameter space (Djorgovski and Davis, 1987; Dressler et al., 1987). This is expected from the virial theorem if a strict homology between all elliptical galaxies is assumed. However, the observed fundamental plane shows a "tilt" with respect to the theorical one: this "tilt" can be explained by non-homology, variations in the stellar population properties (in particular the IMF) and different dark matter fractions, although the relative importance of these effects is still widely debated (Humphrey and Buote, 2010, and citations therein). In particular, the projection of the fundamental plane indicates that the binding energy per unit mass increases with the stellar (or galactic) mass, $\sigma_0 \propto M^{0.32}$ (Faber et al., 1997), i.e. the hot interstellar gas is less bound in low-mass elliptical galaxies. This uniformity is helpful in interpreting the X-ray emission from the hot gas.

1.2.3 The $L_X - L_{opt}$ correlation

Another observational feature is the correlation between the X-ray and the optical luminosities.
In particular, for elliptical galaxies with low optical luminosities ($L_B \lesssim 3 \times 10^9 L_\odot$), O'Sullivan et al. (2001) found that there is approximately a direct proportionality between the bolometric X-ray and B-band luminosities ($L_X \propto L_B$), while they seems to vary approximately as $L_X \propto L_B^2$ for more optically luminous galaxies (Fig. 1.3). These different trends can be explained because low L_B galaxies are apparently dominated by low-mass X-ray binaries with a different (typically harder) spectrum with respect to that of the hot interstellar gas (Brown and Bregman, 2001; Diehl and Statler, 2007).
Moreover, this correlation shows an apparently large scatter (Ellis and O'Sullivan, 2006) which has received much attention. There have been many attempts to relate this scatter to the environment: some authors have found that ellipticals having other massive galaxies nearby have systematically lower L_X/L_B (White and Sarazin, 1991; Henriksen and Cousineau, 1999), whereas others found a positive correlation with L_X/L_B and the local density of galaxies

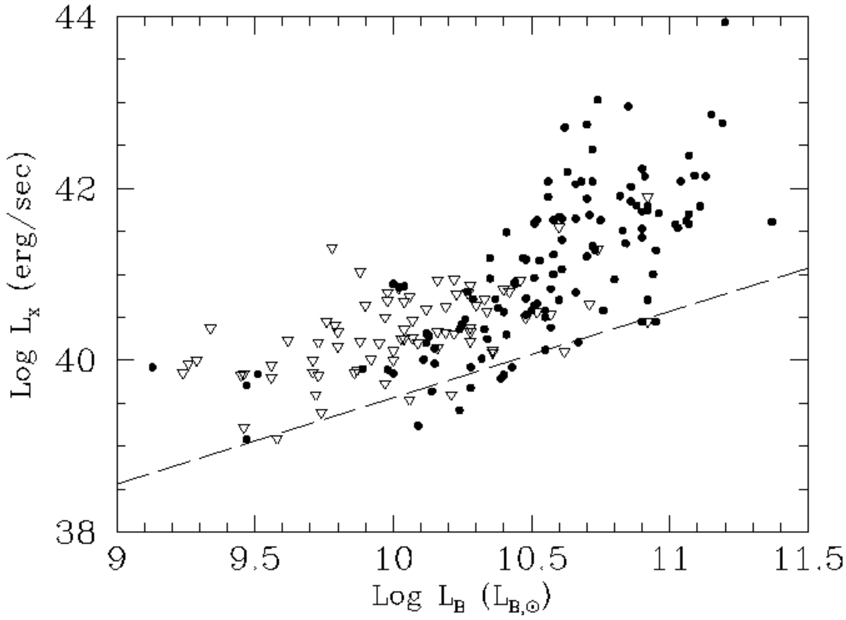

Figure 1.3: B-band optical luminosity versus X-ray bolometric luminosity for O'Sullivan et al. (2001) catalogue. X-ray detections are shown with filled circles, while open triangles are upper limits. The dashed line is an approximate locus of $L_{X,*} \propto L_B$, where $L_{X,*}$ is the total X-ray luminosity of stellar and discrete sources. The plot is taken from Mathews and Brighenti (2003a).

(Brown and Bregman, 2001). Anyway, the scenario can be less simple: in fact, for galaxies in groups or clusters, the environment can act to mantain (or even enhance) a hot halo in some galaxies by an additional contribution of the ambient gas (Helsdon et al., 2001; Mulchaey and Jeltema, 2010), or remove it in other cases by ram-pressure stripping (Toniazzo and Schindler, 2001; Mulchaey and Jeltema, 2010). On the other hand, Mathews et al. (2006) found that the large scatter for group-centered elliptical galaxies of similar optical luminosity can be explained by a large cosmic variation in the surrounding dark halo mass. L_X does, as a matter of fact, correlate with M_{vir}, simply because smaller halos contain fewer baryons, less hot gas, thus having lower L_X.

Nongravitational heating from supernovae and from accretion on the central supermassive black hole also seems to play a fundamental role on the "shape" of this correlation (Mathews et al., 2005, 2006; Diehl and Statler, 2007).

1.2.4 The galaxy mass determination

X-ray observations of the hot gas can also be used to determine the total mass of the galaxy it surrounds. The total mass can be estimated from stellar velocities or gravitational lensing, but the X-ray gas allows, in principle, a even better determination of the mass profile to very large radii. High quality X-ray observations of the gas density and (especially) temperature profiles, like those obtained with the state-of-the-art satellites (see Fig. 1.2), are required and hydrostatic equilibrium must be assumed. In Sec. 4.3.1 I will show that this is, in general, a valid assumption.
To a first approximation, the hydrostatic equilibrium condition

$$\frac{dP_{tot}}{dr} = -\frac{GM\rho}{r^2}$$

leads to the formula (Mathews and Brighenti, 2003a):

$$M(r) = -rT(r)\frac{k_b}{G\mu m_p}\left[\frac{d\log\rho}{d\log r} + \frac{d\log T}{d\log r}\right]. \tag{1.3}$$

In addition to the gas pressure P, a turbulent, magnetic or cosmic rays nonthermal pressure P_{nt} may be present. This nonthermal pressure gives a further term

$$-rT(r)\frac{k_b}{G\mu m_p}\frac{P_{nt}}{P}\frac{d\log P_{nt}}{d\log r}$$

to equation 1.3. Brighenti and Mathews (1997) showed the importance of this non-thermal pressure support for the center of NGC 4636, while (Churazov et al., 2008) found that the combined contribution of cosmic rays, magnetic fields and microturbulence is $\lesssim 10-20$ per cent of the gas thermal energy.

1.2.5 Metal abundances

Finally, the metal abundances of the X-ray hot gas give us many informations on the enrichment history and, consequently, on the IMF and the star formation and evolution in elliptical galaxies.
Many measurements of the metal abundances has been performed over the years leading to many problems, mainly linked to the so called "Fe bias" (Buote et al., 1999; Humphrey and Buote, 2006). Several Chandra and XMM measurements of abundances in X-ray bright galaxies and the centers of groups show roughly solar or even slightly supersolar abundances for the

ISM (for example, Xu et al., 2002; O'Sullivan et al., 2003; Buote et al., 2003a). In contrast, very subsolar Z_{Fe} are still being reported in the lowest L_X/L_B systems (for example, Sarazin et al., 2001; Ji et al., 2009). Humphrey and Buote (2006) found, instead, near-solar abundances, with no convincing evidences for Z_{Fe} correlation with the galaxy X-ray luminosity. The abundances profiles (see Fig. 1.4) shows, anyway, a decrease for large radii ($\sim$ 100 kpc), reaching more "cluster-like" values ($Z_{Fe} \sim 0.2 \div 0.4 Z_{Fe,\odot}$) (e.g., Buote et al., 2003a, 2004).

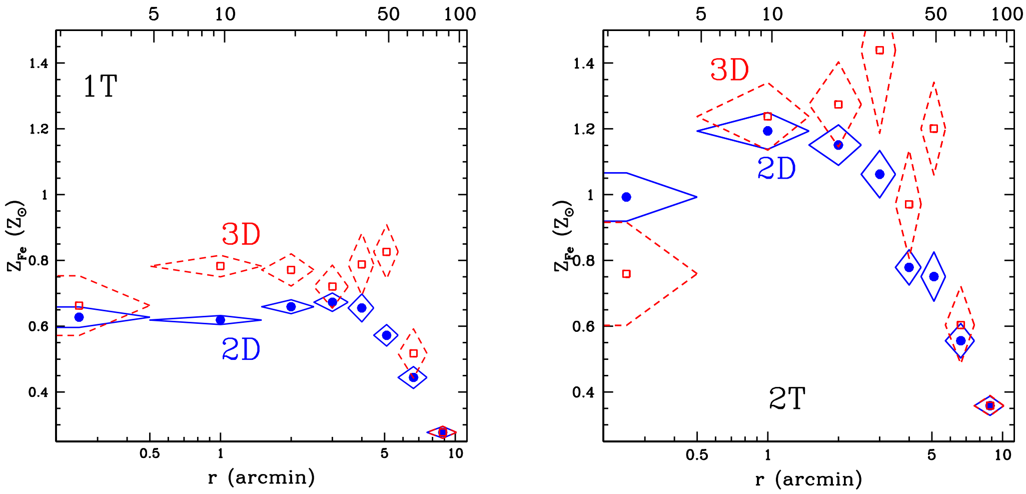

Figure 1.4: Iron abundance profile for NGC 5044 for a single gas temperature model *(left)* and for a two-temperature model *(right)*, fitted simultaneously to the XMM and Chandra data. The so-called "Fe-bias" is clearly visible. Plots are taken from Buote et al. (2003a). The red results have been obtained with a spectral deprojection analysis.

At early times the hot gas was mainly enriched in metals by Type II supernovae formed with the dominant old stellar population. At later times, further enrichment has been provided by Type Ia supernovae and material expelled by old red giant stars (Mathews and Brighenti, 2003a). In group-centered elliptical galaxies, most of the iron produced by Type II supernovae has been dispersed by a galactic wind into distant group gas or nearby intergalactic regions where the gas density is so low that it cannot be observed even with XMM (Brighenti and Mathews, 1999; Mathews et al., 2005). Chandra observations by Martin et al. (2002) of the dwarf starburst wind in NGC 1569 verify that these winds transport almost all of the Type II supernovae enrichment into the local intergalactic medium. Ram-pressure stripping may also be relevant to hot gas enrichment (see, for example, Toniazzo and Schindler, 2001). Finally, ongoing metal-enriched galactic outflows energized by Type Ia supernovae are energetically likely in low luminosity ellipticals. There have been many efforts to exactly model the enrichment of the hot gas. In the traditional "galactic wind models" the galaxies form monolithically and passively evolve; during this time, the dynamics and luminosity of the gas are strongly affected by SN feedback, which can drive periods of large-scale galactic outflow (e.g., Mathews and Baker, 1971; Ciotti et al., 1991). This model, however, seems to overproduce iron in the hot gas (Loewenstein and Mathews, 1991; Humphrey and Buote, 2006). Kawata and Gibson (2003) simulated, with a N-body/SPH code, the evolution of an elliptical galaxy in the hierarchical scenario, but their model predicts $Z_{Fe} \lesssim 0.3$. Even with the inclusion of AGN feedback, they underestimate the observed iron abundances (Kawata and Gibson, 2005). Mathews et al. (2004) found, with an hydrodynamical eulerian code, that a continuous heating from the central AGN could drive "circulation flows" which mix gas through the galaxy. This model seems, indeed, successful in reproducing the actually observed values of Z_{Fe}.

It is clear (and in some cases it has expressly been mentioned) that all the properties of the hot gas in elliptical galaxies are strictly linked to and influenced by the eventual feedback by the supermassive black hole residing in the center of the galaxy. I will treat the effects of this feedback in Chapters 2 and 4.

Chapter 2

The hot gas "cooling problem"

The hot gas in elliptical galaxies and galaxy groups and clusters is expected to cool in the central region of the structure. If the X-ray emission is not compensated by heating, the gas should radiate its thermal and gravitational energy on a typical timescale (for isobaric cooling) of

$$t_{cool} = \frac{5 m_H k_b T}{2 \mu \rho \Lambda(T)}, \tag{2.1}$$

where μ is the mean molecular weight, m_H is the hydrogen mass, k_b is the boltzmann constant and $\Lambda(T)$ is the cooling function (Mathews and Brighenti, 2003a). Computing the central cooling time for eight elliptical galaxies (NGC 4125, NGC 720, NGC 6482, NGC 1407, NGC 4472, NGC 4649, NGC 4261, NGC 4636; data from Humphrey et al. (2006) and Baldi et al. (2009)), this timescale goes from a minimum value of $\simeq 1.6 \times 10^7$ yr to a maximum value of $\simeq 3.6 \times 10^8$ yr, that is much less than the Hubble time (see also Fig. 2.1 for the cooling times of the ICM in clusters of galaxies).

Many authors proposed a simple model to describe this cooling, leading to the classical "cooling flow" paradigm (Sec. 2.1), but XMM and Chandra observations have shown the absence of emission from gas at intermediate or low temperatures. The hot gas radiates, but it doesn't seem to cool.

There are essentially two approches to solve this problem:

a) the gas is cooling, but it is not detected;

b) the gas is heated by some physical phenomenon, so little gas can really cool.

In Sec. 2.2 I will briefly discuss the first hypotesis (severely restricted, if not ruled out entirely by observations), while the second one will be widely

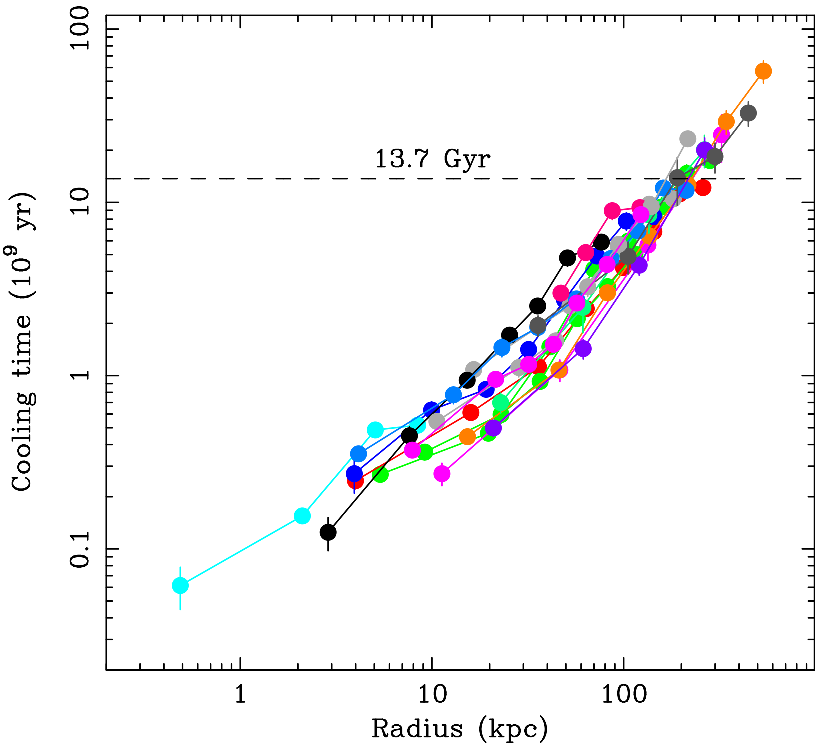

Figure 2.1: The cooling time as a function of radius for the intracluster medium of a sample of clusters of galaxies. The plot is taken from Peterson and Fabian (2006).

treated in Sec. 2.3.

2.1 Classical cooling flows

A classical cooling flow is expected to form when t_{cool} is less than the age of the system ($t_a \sim {H_0}^{-1}$). In this model, t_{cool} exceeds the gravitational free-fall time, t_{grav}, so $t_a > t_{cool} > t_{grav}$ and the gas can be considered in quasi-hydrostatic equilibrium. The flow takes place because the gas density has to rise to support the weight of the overlying gas. The inflow is essentially pressure-driven (Fabian, 1994). To see this clearly, let us consider the gaseous atmosphere trapped in the gravitational potential well of a galaxy (or a group, or a cluster) to be divided in two parts by the cooling radius r_{cool}, where $t_{cool} = t_a$. The gas pressure at r_{cool} is determined by the weight of the overlying gas, in which cooling is not important. Within r_{cool} the temperature lowers because of cooling and the gas density has to rise in order to mantain the pressure at r_{cool}. The gas flows inward, so that, typically, the temperature of the cooling gas follows the underlying gravitational potential, i.e., $k_b T/(\mu m_H)$ is a multiple of order unity of the "local virial temperature", $GM(r)/r$ ($\beta \sim 1$ in Eq. 1.1). Rather than being a direct manifestation of cooling, this temperature drop reveals the flattening of the underlying gravitational potential. The classical cooling flow is approximately steady within the region where the cooling time is shorter than its age ($r < r_{cool}$). The power radiated from the steady flow equals the sum of the enthalpy carried into it and the gravitational energy dissipated within it. The mass deposition rate $\dot{M}$ due to cooling can be estimated from the X-ray images by using the luminosity associated with the cooling region; assuming that it is all due to radiation of the thermal energy of the gas plus the PdV work done on the gas that is inflowing:

$$L_{X,cool} \approx \frac{5k_bT}{2\mu m_H}\dot{M} \approx 10^{41} T_7 \frac{\dot{M}}{M_\odot\ yr^{-1}} erg\ s^{-1} \tag{2.2}$$

This expression is exact for steady, isobaric cooling. The lack of such predicted luminosities, along with its failure to predict the observed amount and spatial distribution of star formation, line emission, and other expected products of cooling, forced astrophyicists to update this scenario.

2.2 How to hide the cool gas?

Most of the evidence that cooling is incomplete or absent comes from XMM RGS (reflection grating spectrometer) spectra of cluster scale flows.
For Abell 1835, a massive cluster with $T_{vir} \approx 9\ keV$, Allen et al. (1996) estimated a large mass deposition rate, $\dot{M} \approx 2000\ M_\odot\ yr^{-1}$, using an X-ray image deprojection procedure based on a steady state cooling flow model. This cooling rate has now been adjusted downward to $\dot{M} < 200\ M_\odot\ yr^{-1}$ because the XMM RGS spectrum of Abell 1835 shows no emission lines from ions at temperatures $T < T_{vir}/3$ (Peterson et al., 2001). Similar drastic reductions were made to morphological $\dot{M}$ estimates for other clusters; in these clusters, the gas temperature drops from T_{vir} at large radii to about $\lesssim T_{vir}/3$ near the center, with little or no indication of multiphase (cooling) gas at lower temperatures, $kT \lesssim 1 - 2\ keV$.
Even for galaxy/group flows the spectroscopic $\dot{M}$ also seems to be significantly lower than the morphological $\dot{M}$, as in cluster flows. XMM RGS observations of NGC 4636 by Xu et al. (2002) indicate that the gas temperature decreases from $8.1 \times 10^6\ K$ at 3 kpc to $6.4 \times 10^6\ K$ at the center, but there is little or

no spectroscopic evidence for gas emitting at temperatures $< 6 \times 10^6$ K. The OVII line at 0.574 keV that emits near 2.5×10^6 K is not detected.

In view of the failure to detect significant cooling at X-ray temperatures, it is remarkable that faint, diffuse, warm gas at $T \sim 10^4$ K ($H_\alpha + [NII]$) is indeed observed near the centers of groups and clusters formerly identified as cooling flows, but the mass of warm gas ($10^4 \div 10^5 M_\odot$) is very much less than the mass that would have cooled in the classical cooling flow scenario. This diffuse warm gas that emits optical emission lines could have been recently ejected from stars, cooled from the hot phase, acquired in a recent galactic merger, or accreted from local gas clouds similar to the high velocity clouds that fall toward the Milky Way (Mathews and Brighenti, 2003a).

The spectral contributions of cooling gas can be reduced if the X-ray emission from the cooling gas is absorbed or if the cooling is more rapid than normal radiative cooling (Peterson et al., 2001; Fabian et al., 2001).

Column densities N_H of a few 10^{21} cm^2 are sufficient to absorb X-rays with energy ~ 1 keV, provided the absorbing gas is reasonably cold, $T \lesssim 10^6$ K. Buote (2000a,b, 2001) and Allen et al. (2001) reported evidence for an absorbing oxygen edge (at $\sim$ 0.5 keV) and intrinsic absorbing columns $N_H \sim 10^{21}$ cm^2 within $\sim 5 - 10$ kpc in several bright elliptical galaxies, such as NGC 5044 and NGC 1399. Unfortunately, the mass of absorbing gas required to occult the central regions of these galactic flows is too large and it is unclear how this (necessarily colder) gas would be supported in the galactic gravity field and how it would escape detection at other frequencies (Voit and Donahue, 1995). Further, absorbing gas with $N_H \gtrsim 10^{20}$ cm^2 would produce observable reddening of the background stars and large far-infrared luminosities unless the gas is dust-free. Even XMM and Chandra spectra of the nonthermal nucleus and jet of M87 and the nucleus of NGC 1275 fail to show intrinsic X-ray absorption at the level required to mask cooling in the thermal gas (Böhringer et al., 2001). Perhaps the ideal X-ray absorption model would be one in which the cooling regions are themselves optically thick at $\lesssim 1$ keV, but the attempts to achieve this have been unsuccessful.

If the cooling rate at $kT \lesssim 1$ keV were somehow accelerated, the X-ray emission from cooling gas would be reduced. Begelman and Fabian (1990) and Fabian et al. (2001) propose that hot gas (at T_{hot}) may rapidly mix with cold gas (at T_{cold}) and thermalize to $T_{mix} \sim (T_{hot} T_{cold})^{1/2}$ with little emission from temperatures $T_{hot} > T > T_{mix}$. Assuming $T_{hot} \sim 10^7\ K$ and $T_{cold} \sim 10^4\ K$, then $T_{mix} \sim 3 \times 10^5\ K$. One potential difficulty with this process is that the warm gas ($\sim 10^4\ K$) in elliptical galaxies has a filling factor of only $\sim 10^{-6}$ (see, for example, Mathews, 1990), so it is not plausible that the hot gas can find enough cold gas to mix with (neutral and molecular gas at $T < 10^4\ K$ are also in short supply). In any case, when the gas at $T_{mix} \sim 3 \times 10^5\ K$ cools further, it should radiate strongly in the OVI UV doublet, which, at least for NGC 1399, is not observed. In any case, the soft X-ray emission missing from cooling regions should appear somewhere else in the spectrum (Fabian et al., 2002).

Fujita et al. (1997) and Fabian et al. (2001) proposed cooling flow models with inhomogeneous metal abundances. In this scenario, regions of enhanced iron abundance, possibly enriched by individual Type Ia supernovae, cool rapidly, reducing the X-ray line emission from intermediate temperatures, while the remaining gas of lower metallicity can also cool, but with low line emission. This is an elegant solution, but it is difficult to explain this inhomogeneity.

Finally, Mathews and Brighenti (2003b) discussed the role of dust in the cooling process. They modeled the thermal evolution of dusty gas ejected from red giant (AGB) stars in E galaxies in which the gas is first rapidly heated to the ambient temperature, $\sim 1\ keV$, then cools by thermal electron collisions with the grains. The electron-grain cooling time is indeed shorter than normal plasma cooling time, the local galactic dynamical time, and the grain sputtering time. Extended far-infrared emission from dust is effectively observed in several elliptical galaxies, but the emission does not correlate with the X-ray luminosity and the extension of this FIR emission can be, instead, well explained by circulation flows induced by buoyantly rising gas intermittently heated by low-luminosity active galactic nuclei (Temi et al., 2007a,b).

2.3 Heating the gas

Of course, to solve the "cooling problem" it may be simpler to assume some form of heating, counterbalancing the expected cooling.

Many different models have been proposed throughout the years for both the hot ISM of elliptical galaxies and the ICM. Mathews and Baker (1971) modelized supernovae driven galaxy winds; supernovae, indeed, play an important role in heating the gas, but they are not sufficient in terms of energy amount and in reproducing the shape of the global temperature and density profiles.

Tucker and Rosner (1983) and Loewenstein et al. (1991) studied heating by thermal conduction coupled with diffuse cosmic rays producing Alfven waves as they stream along the magnetic field lines. It is still uncertain if and how much magnetic fields can suppress thermal conduction, but it could be helpful in heating the outer regions of the halo. Cosmic rays are effective at small radii, but they produce too much nonthermal pressure and still cannot balance radiative cooling.

Tabor and Binney (1993) develop a steady-state flow in which a central heating source leads to a convective core that is attached to an outer cooling inflow. However, the central temperature gradient is always negative (contrary to observations), because it is determined by the gravitational potential ($dT/dr = -(2\mu m_H)/(5k_b)(d\Phi/dr)$; see Mathews and Brighenti, 2003a).

This is only a little (even if well rapresentative) sample of a great and differed variety of models, many of them are directly or indirectly associated to a “nongravitational” heating. In particular, the entropy of the hot gas could be a tracer of “nongravitational” heating. Using ROSAT data, Lloyd-Davies et al. (2000) found an “entropy floor” in the $S-T$ relation (where $S \equiv T/{n_e}^{2/3}$ is the “entropy factor”) for groups and clusters; this means that the gas in elliptical-dominated groups has somehow acquired an additional “entropy” of $\sim 100\ keV\ cm^2$ in excess of that received in the cosmic accretion shock near the virial radius. In particular, an early “preheating” by $\sim 1\ keV$/particle could explain this anomalous behavior in the $S-T$ relation for groups, since heating at early cosmic times, when the density is low, can increase the gas entropy with a smaller energy expenditure (Mathews and Brighenti, 2003a). With higher resolution data from Chandra, the entropy floor is no longer seen, but there is an apparent excess of entropy at larger radii, beyond the inner cooling region (McNamara and Nulsen, 2007). In sum, there is still a wide debate on this topic, but supernovae and AGNs are actually a good explanation for this entropy excess for “colder” structures (e.g., Tornatore et al., 2003; Davé et al., 2008).

2.3.1 AGN heating: why

AGN, in principle, can provide enough energy to balance the total energy radiated from galactic/group cooling flows, $L_X \sim 10^{41.5\pm1}$ $erg\ s^{-1}$.

There are, indeed, several observational features that are explained invoking AGNs.

For example, Croton et al. (2006) studied the impact of AGN feedback on galaxy formation and evolution. Running a high-resolution cosmological simulation, he found that a "quasar" accretion on the central black hole, mainly driven by major mergers, can explain the observed relationship between the mass of the bulge of galaxies and the mass of the central black hole. On the other hand, a continous and quiescient "radio" accretion mode is very helpful in reproducing, in addition to the observed degree of suppression of cooling flows, the galaxy luminosity function (with a sharper high-mass cut-off) and, by affecting the star formation history, the mean stellar ages of galaxy systems and the colour distribution of galaxies, with red, elliptical galaxies as most massive systems.

Pope (2009) constructed a simple analytical model to investigate the effects of mechanical and thermal feedback of AGN on the $L_X - \sigma$ $(L_X - T)$ relation for elliptical galaxies, groups and clusters. He found that if the black hole is fuelled at a rate proportional to the classical mass cooling rate ($\dot{M} \propto L_X/\sigma^2$, see Eq. 2.2), $L_X \propto \sigma^{10}$ for lower mass galaxies and $L_X \propto \sigma^7$ for higher mass galaxies and groups, while if the fuelling rate is simply proportional to the X-ray luminosity, $L_X \propto \sigma^8$ for lower mass galaxies and $L_X \propto \sigma^5$ for higher mass galaxies and groups. These different trends for systems with different mass depend on the fuelling mechanism, with a "kinetic" feedback dominating at lower masses and a "thermal" feedback dominating at higher masses. The effects of AGN heating on $L_X - T$ relation are also (at least qualitatively) confirmed by semi-analytic models and simulations (Tornatore et al., 2003; Bower et al., 2008; Davé et al., 2008).

As told in advance, in Sec. 1.2, AGN is also expected to play a significant role in the large scatter observed in the $L_B - L_X$ relation for elliptical galaxies. Mathews et al. (2005) performed a simple calculation on NGC 5044, finding that an accretion on the central black-hole, with efficiency of $\sim$ 10%, is sufficient to explain the deviation from a self-similar relationship without expelling all the gas from the system. In addition, this heating of $\simeq 1$ keV

per particle is consistent with the amount of energy required for the entropy excess discussed in Sec. 2.3.

Finally, Diehl and Statler (2007) found that the hot gas distribution in elliptical galaxies is much more disturbed than the stellar one. In particular, in a following paper (Diehl and Statler, 2008a) they found that the asimmetry index η, which measures the statistical deviation from an X-ray symmetric surface brightness model, correlates with the total radio power and the luminosity of the X-ray central point source.

Of course, these findings are noway strongly supported by many high-resolution Chandra images that reveal a great assortment of structural disturbances near the flow centers where supermassive black holes should be activated by the inflowing gas (see Fig. 2.2, but also Fig. 3.1).

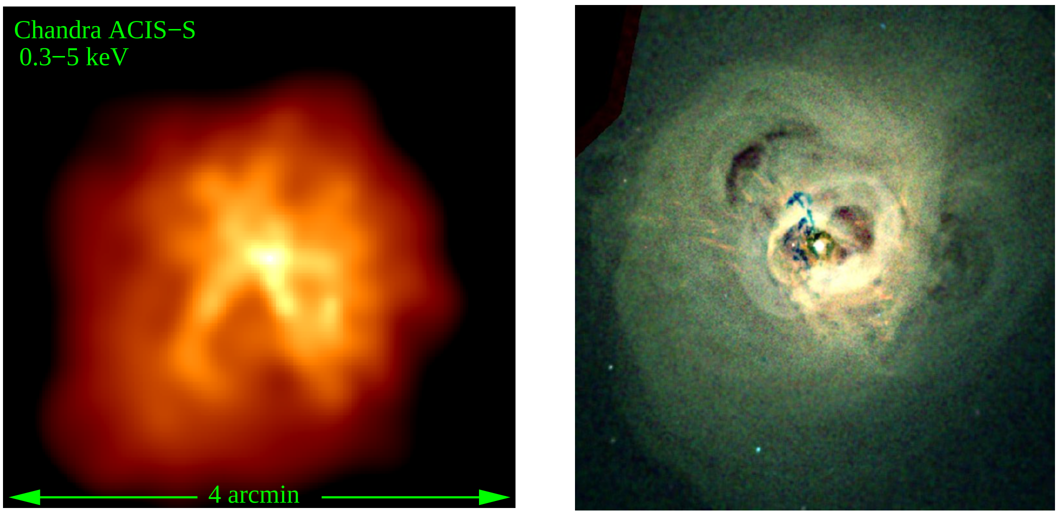

Figure 2.2: Left: Chandra image of the center of NGC 5044, taken from Buote et al. (2003b). Right: Chandra image of the center of the Perseus cluster, taken from Fabian et al. (2006).

2.3.2 AGN heating: how

In order to prevent significant gas cooling, a self-regulated AGN feedback should be activated with a frequency of the order of $\approx 1/t_{cool}$. Moreover, the feedback heating must preserve the cool core appearance of the hot gas distribution: concentrated and isotropic heating can be too efficient and it often generates negative central temperature gradients, so a "directional" input of energy, such as jets or collimated ouflows, is often invoked.

Of particular interest are the X-ray cavities, regions of much lower thermal emission. These cavities are believed just to be formed by such collimated interaction. They are, in fact, often coincident with radio lobes, even if there are also “ghost cavities”, at larger distances from the galactic center, that no longer produce ($\sim GHz$) radio emission. Anyway, whether the cavities are dominated by thermal or nonthermal plasma, they must be buoyant on timescales $t_{buoy} \sim 10^7 - 10^8\ yr$ (Mathews and Brighenti, 2003a). Most of Chandra observations are of cluster-centered, elliptical galaxies having strong radio sources, but similar hot gas cavities are also apparent in the centers of more normal, group-centered E galaxies and they seem to be an almost universal phenomenon, as shown by McNamara and Nulsen (2007) (see Fig. 2.3).

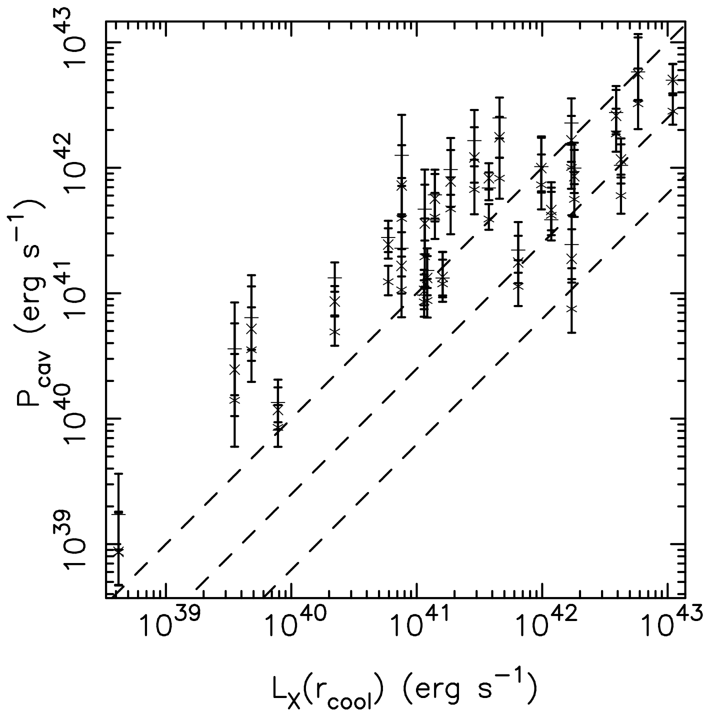

Figure 2.3: Cavity power versus cooling power for nearby giant elliptical galaxies. See McNamara and Nulsen (2007) for details.

McNamara and Nulsen (2007) described three main heating mechanisms associated with AGN feedback. The first one involves the buoyancy of the cavities. Simulations show that buoyant cavities can heat the surrounding gas as they rise through a cluster atmosphere (see, for example, Brüggen and Kaiser, 2002). In McNamara and Nulsen (2007) model, as a buoyant cavity rises, some X-ray emitting gas must move inward to fill the space it vacates, so that gravitational potential energy is turned into kinetic energy in the surrounding medium. The potential energy released as a cavity rises an infinitesimal distance δR is

$$\delta U = Mg\delta R = \rho V g\delta R = -V\frac{dp}{dR}\delta R = -V\delta p \tag{2.3}$$

where ρ is the density of the surrounding gas, $M = \rho V$ is the mass of gas displaced by the cavity, V is its volume and g is the acceleration due to gravity. The third equality relies on the surrounding gas being close to hydrostatic equilibrium, so that $\rho g = -dp/dR$. The last equality expresses the result in terms of the change in pressure of the surrounding gas over the distance δR, $(dp/dR)\delta R = \delta p$. The "rising velocity" of the cavity is

$$v_{buoy} = \left(\frac{8r_{cav}}{3RC}\right)^{1/2} v_K,$$

where r_{cav} is the cavity radius, R is the distance from the galactic center, C is a "drag" numerical coefficient and $v_K = (gR)^{1/2}$ is the Keplerian velocity. Because the rising cavity moves subsonically (Churazov et al., 2001), δp can be seen as the change in pressure the cavity experiences to readjust to pressure equilibrium with the surrounding gas. The first law of thermodynamics, $dE = TdS - pdV$, can be expressed in terms of the enthalpy, $dH = TdS + Vdp$. Entropy remains constant for an adiabatic cavity (radiative losses from the cavity are negligible), so that this gives $\delta H = \delta V p$. Thus, Eq. 2.3 shows that the kinetic energy created in the wake of the rising cavity is equal to the enthalpy lost by the cavity as it rises. Kinetic energy is then damped before diffusing far from the axis on which the cavity rises, so the enthalpy lost by a buoyantly rising cavity is thermalized locally in its wake. In terms of mean heating rate over the "spherical" lobe, this model gives

$$\Pi_{buoy} = -\frac{L_b}{4\pi R^2}\frac{d}{dR}\left(\frac{p}{p_0}\right)^{(\Gamma-1)/\Gamma}, \tag{2.4}$$

where L_b is the luminosity (power) injected in the cavity as enthalpy, Γ is the ratio of specific heats for the gas filling the cavity and p_0 is the pressure at the location of the cavity formation.

The second model proposed by McNamara and Nulsen (2007) involves weak shocks. For weak shocks, the entropy jump per unit mass, S, is proportional to the cube of the shock strength (here measured as the fractional pressure increase $\delta p/p$). The equivalent heat input per unit mass is $T\Delta S$, where T is the gas temperature. To lowest nonzero order, this equivalent heat input amounts to a mean heating rate per unit volume due to repeated weak shocks of

$$\Pi_{sh} = -\frac{\gamma+1}{12\gamma^2}\frac{\omega_{sh}p}{2\pi}\left(\frac{\delta p}{p}\right)^3, \tag{2.5}$$

where γ is the ratio of specific heats for the hot gas, while $\omega_{sh}/2\pi$ is the frequency of the outbursts.

The third model involves sound damping and it is, in some way, similar to the previous one. Repeated weak shocks may also be regarded as a superposition of sound waves. The heating power per unit volume due to dissipation of a sound wave can be expressed as

$$\Pi_{damp} = -\left[\frac{2\nu}{3} + \frac{(\gamma-1)^2\kappa T}{2\gamma p}\right]\frac{\omega^2\rho}{\gamma^2}\left(\frac{\delta p}{p}\right)^2, \tag{2.6}$$

where κ is the thermal conductivity, ν is the kinematic viscosity ($\nu = \eta/\rho$, where η is the viscosity), ω is the angular frequency, and δp is the pressure amplitude of the sound wave. This expression includes both viscous and conductive dissipation. Both terms in the leading coefficient have the form of a mean free path times a thermal speed. For an unmagnetized plasma, the mean free paths of the electrons and protons are the same. For the kinematic viscosity, the thermal speed is that of the protons, whereas in the conductive term it is that of electrons. Thus conductive dissipation would be greater in the absence of a magnetic field.

Many high-resolution hydrodynamic simulations have been performed in the last years, mainly focusing on these effects of jets and cavities on the intracluster medium (see, for example, Gaspari et al. (2011) and references therein). It is particularly interesting to perform similar simulations on the smaller galactic scales, for the hot interstellar medium in elliptical galaxies.

Chapter 3

An insight on the unusual X-ray morphology of NGC 4636

This chapter is dedicated to Baldi et al. (2009) study on the X-ray emission of NGC 4636. NGC 4636 is a giant elliptical galaxy at a distance of $\sim 16\ Mpc$[1] in the southern border of the Virgo cluster, about 3 Mpc from the center (Chakrabarty and Raychaudhury, 2008). Furthermore it lies on the center of a poor group of which it is the brightest galaxy (Osmond and Ponman, 2004).

This galaxy has been observed extensively by every major X-ray observatory from Einstein, ROSAT and ASCA to more recent XMM-Newton and Chandra satellites; it is found to be very bright in this region of the electromagnetic spectrum, $L_X \sim 10^{41}\ erg/s$, with unusual morphology in the core (Jones et al., 2002; O'Sullivan et al., 2005).

3.1 X-Ray Chandra observations: global properties and the arm-like features

Enhancing the previous works, Baldi et al. (2009) performed a study of NGC 4636 in the X-ray band, focusing on its particular morphology. They used three different Chandra observations performed with ACIS-S (2000, January 26) and ACIS-I (2003, February 14 and 2003, February 15), for a total exposure time of $\sim 200\ ks$; Fig. 3.1 shows the merged $0.3 - 2\ keV$ image of all these observations.

Fig. 3.2 shows the obtained surface brightness profile. The galaxy presents a bright central core of radius $\sim 1\ kpc$ without a central peak and a diffuse emission region with lower surface brightness extending out to $\sim 6\ kpc$, showing

[1] Distance taken from NED, http://nedwww.ipac.caltech.edu/.

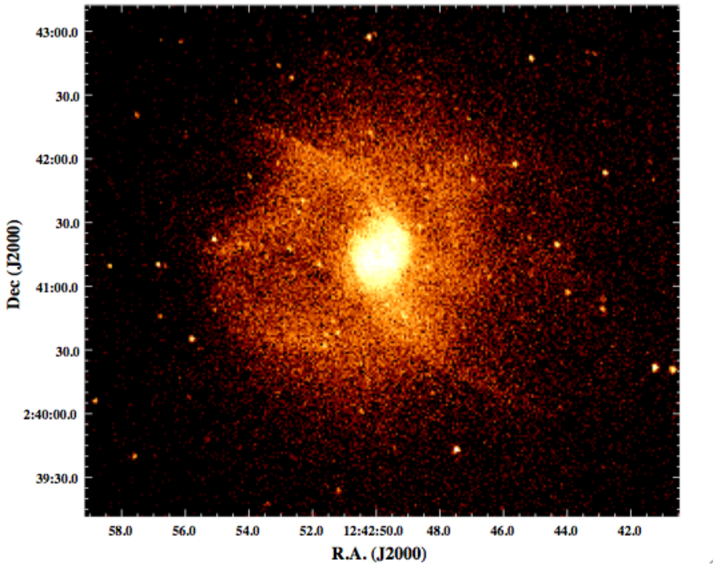

Figure 3.1: Chandra ACIS-I+ACIS-S image of NGC 4636 in the $0.3 - 2\ keV$ band. Two quasi-symmetric (8 kpc long) arm-like features are clearly visible.

a plateau at $1.5\ kpc \lesssim r \lesssim 4\ kpc$. Both these features are also visible in Fig. 3.1.

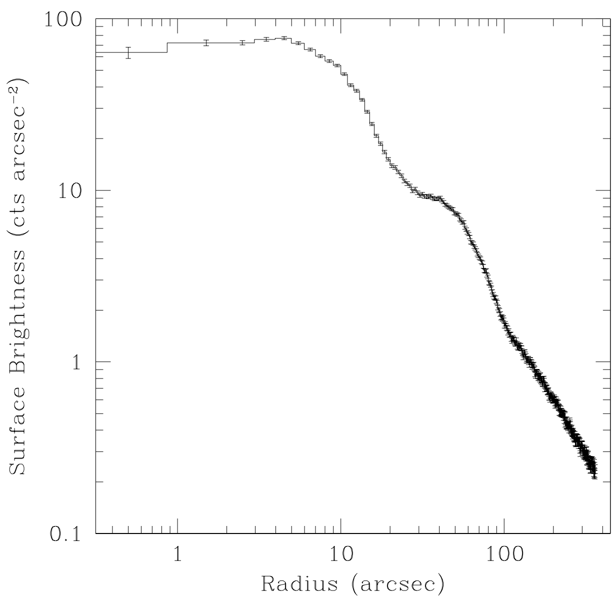

Figure 3.2: X-ray surface brightness profile for NGC 4636, extracted in the band $0.3 - 5\ keV$. Here $1'' \approx 70\ pc$

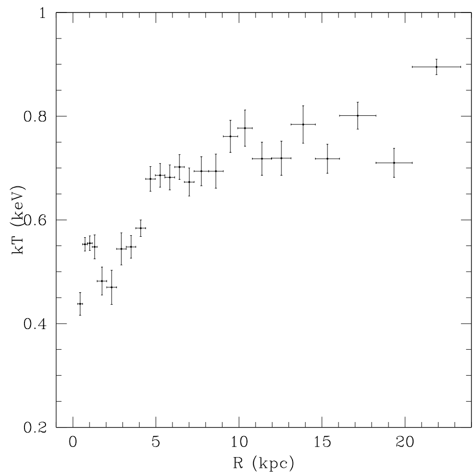

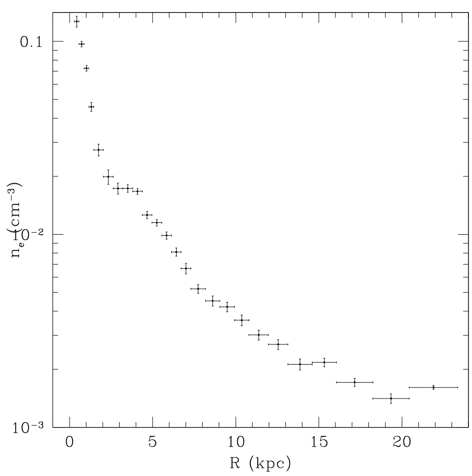

Figure 3.3: Left: deprojected temperature profile for hot gas in NGC 4636. Right: deprojected electron number density profile for hot gas in NGC 4636.

Deprojected temperature and electron number density profiles are shown in Fig. 3.3. In the spectral analysis, Baldi et al. (2009) found no abundance profile trend (in accordance with O'Sullivan et al. (2005)), so they decided to fix $Z = 0.5\ Z_{\odot}$. As in other giant elliptical galaxies (see, for example, Mathews and Brighenti, 2003a), the temperature shows a clear decrease toward the center, where $kT \sim 0.5$, while it increases to $kT \gtrsim 0.8$ toward the outskirts of the galaxy. The electron density is, instead, centrally peaked, with a plateau corresponding to that observed in the surface brightness.

Maybe the most interesting property of NGC 4636 is the presence of two quasi-simmetric arm-like features embedded in the surface brightness emission (see Fig. 3.1). As better explained in Sections 3.2 and 3.3, these features are believed to be part of three different cavities, better visible after the subtraction of a β-model (Sarazin, 1986)

$$I_X(r) \propto (1 + (r/r_c))^{3\beta+1/2}, \tag{3.1}$$

fitted to the galaxy diffuse emission (see Fig. 3.4). In support of this hypotesis, there is also a correlation between the cavities and the radio data, although the plasma eventually creating the cavities remains partially undetected (see Fig. 3.5).

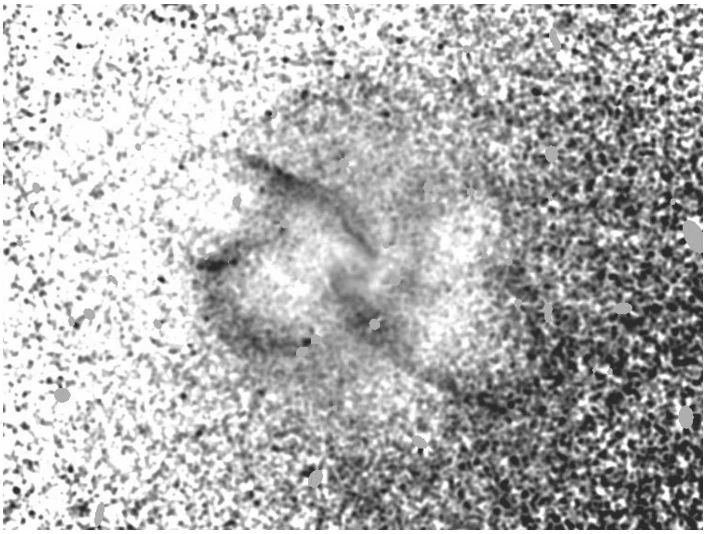

Figure 3.4: Chandra ACIS-I+ACIS-S image of NGC 4636 after the subtraction of a β-model fitted to the galaxy diffuse emission. The arm-like features seem to be the rims of (two or) three cavities

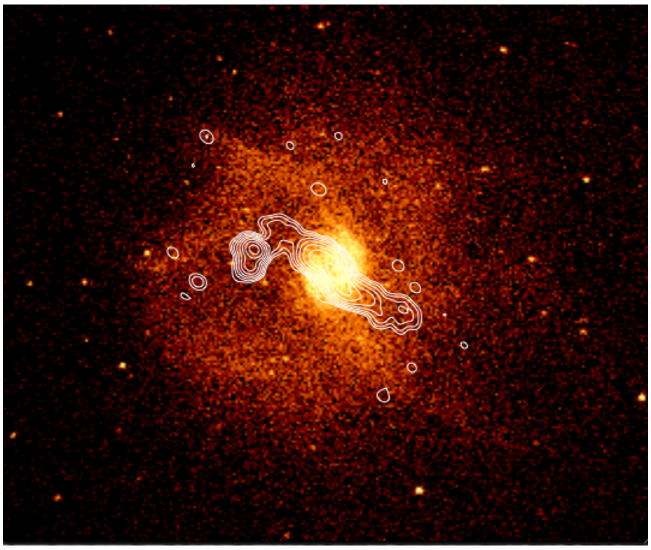

Figure 3.5: 610 MHz GMRT radio contours superimposed on the Chandra ACIS-I+ACIS-S $0.5 - 3$ keV image.

3.2 The cavities: a spectral analysis

As told in advance, Baldi et al. (2009) believe the arm-like X-ray structures to be the rims of three bubbles. Fig. 3.6 shows the contours of these bubbles, hereafter SW, NE and E bubbles, accounting for their location with respect to the center of NGC 4636. In order to explain the origin and nature of the cavities, Baldi et al. (2009) studied them in detail, performing a spatially resolved spectral analysis.

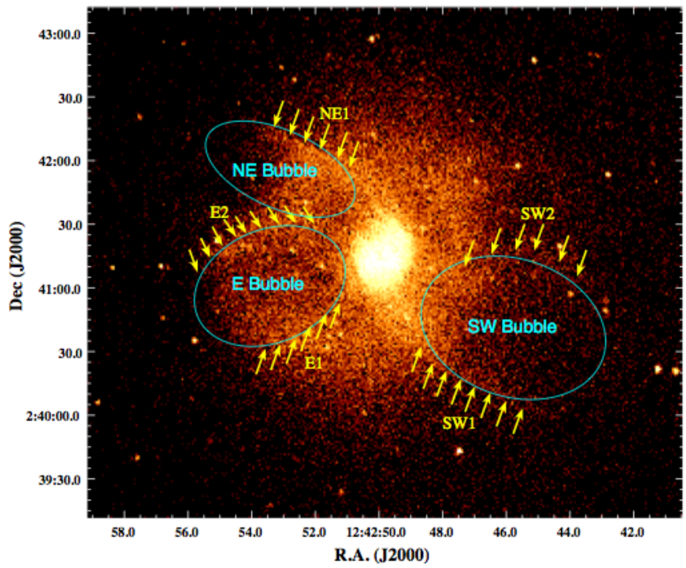

Figure 3.6: Chandra ACIS-I+ACIS-S image of NGC 4636 in the $0.3 - 2\ keV$ band. The contours of the three detected bubble-like features are highlighted in cyan. The yellow arrows point toward the detected rims.

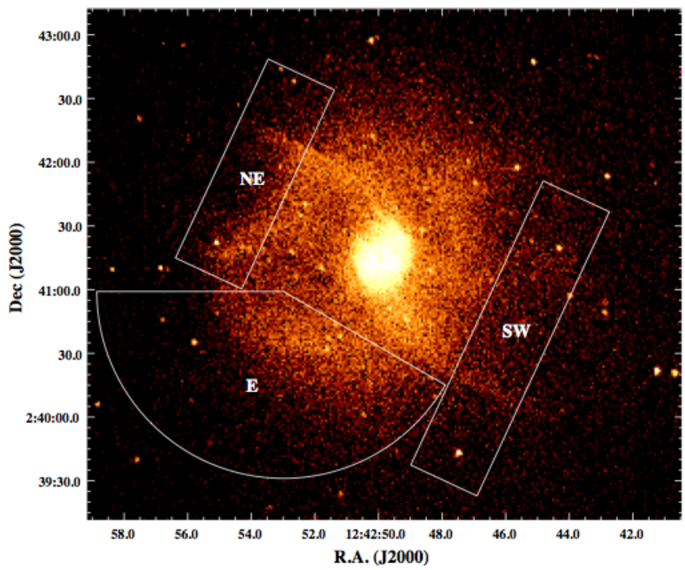

Figure 3.7: Chandra ACIS-I+ACIS-S image of NGC 4636 in the $0.3 - 2\ keV$ band. The regions used by Baldi et al. (2009) to perform the spectral analysis of the three bubble-like features are highlighted in white.

3.2.1 The SW bubble

The arm-like feature in the southwest region of NGC 4636 (SW1 in Fig. 3.6) seems to be the southern rim of a cavity extending at least $\sim 5\ kpc$ to the north, altough a northern rim (SW2 in Fig. 3.6) is not as well defined as the southern one. Baldi et al. (2009) performed a spectral analysis for the cavity, defining a strip perpendicular to SW1 and dividing it into $\sim 0.5'$ wide rectangles (see Fig. 3.7). Fig. 3.8 shows the surface brightness profile across the SW bubble. The metallicity does not vary significantly across the bubble rim, while a sharp jump in temperature is detected for SW1, with temperature decreasing from $kT \sim 0.75\ keV$ to $kT \sim 0.64\ keV$, the difference being well above measurement errors (see Fig. 3.8). For SW2, strangely, Baldi et al. (2009) did not find a temperature jump in corrispondence to the surface brightness observed one.

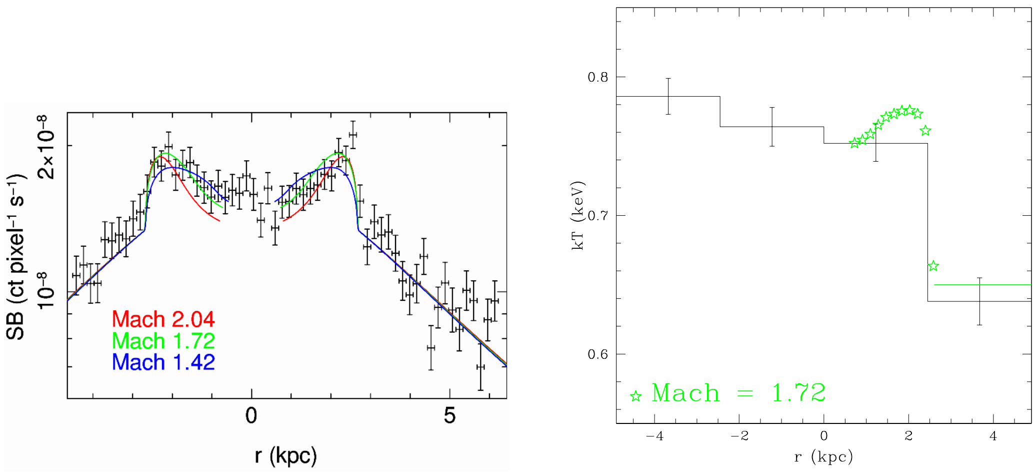

Figure 3.8: Left: surface brightness profile across the SW bubble; the three colored solid lines show the predicition for the hydrodynamical simulation performed by Baldi et al. (2009) and described in Sec. 3.3, at different Mach numbers for the shock. Right: temperature profile across the SW bubble; the green stars show the profile expected for a shock simulation with Mach number $M = 1.72$. The zero points in r are coincident with the center of the rectangle in Fig. 3.7 and r increases toward the south.

3.2.2 The NE and E bubbles

The surface brightness profile for the NE bubble is similar in shape to the SW one (see Fig. 3.9). The spectral analysis, for this cavity, is performed in a way equivalent to that described in Subsection 3.2.1 for the SW bubble (see also Fig. 3.7). Also a temperature jump across NE1 rim in Fig. 3.7 is detected, as shown in Fig. 3.9.

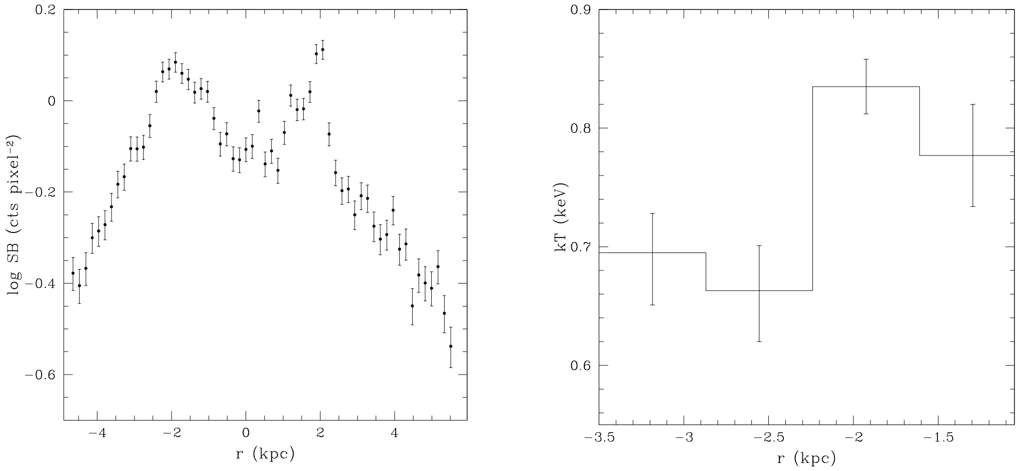

Figure 3.9: Left: surface brightness profile across the NE bubble. Right: temperature profile across the NE1 rim in Fig. 3.7. The zero points in r are coincident with the center of the rectangle in Fig. 3.7 and r increases toward the south.

For the E cavity, because of a possible contamination from the NE cavity, the spectral analysis is performed only for the E1 rim, using 5 partial annuli instead of rectangles (see Fig. 3.7). The surface brightness profile is similar to the previous ones and a temperature jump is detected in coincidence of this rim (see Fig. 3.10).

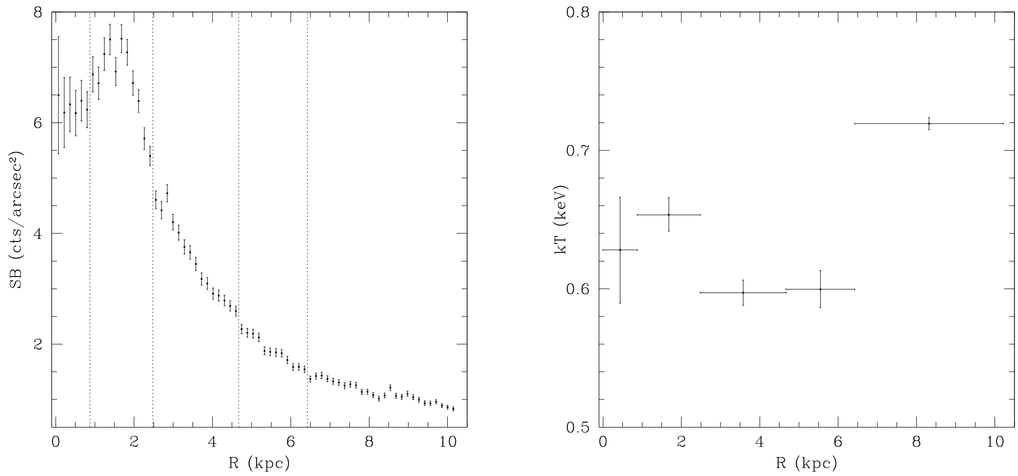

Figure 3.10: Left: surface brightness profile across the E1 rim in Fig. 3.7; the dashed vertical lines delimitate the regions used by Baldi et al. (2009) for the spectral analysis. Right: temperature profile across the E1 rim. The zero points in r are coincident with the central vertex of the circular slice in Fig. 3.7.

3.3 A model for the origin of the cavities

Baldi et al. (2009) proposal to explain such cavities is that they are the result of an outburst from the central AGN. In this scenario, the jet is believed to rapidly propagate, creating a long and thin cavity which then inflate in all directions. In this case, perpendicular to the axis of the jet, the inflation has an approximate cylindrical simmetry, which also motivates the choice of rectangular regions to perform spectral analysis of the bubbles.

The idea is that the expanding cavities drive shocks into the surrounding gas, so Baldi et al. (2009) used a one-dimensional, cylindrically symmetric, time-dependent hydrodynamic model to investigate the properties of these shocks for the SW bubble. In this model, the assumption is that the sound speed of the relativistic gas in the cavity is very high, ensuring that the expansion pressure is nearly uniform. The strength of the shock is determined by the ratio between pre-shock and post-shock pressure. So, as a result of the gas pressure distribution, the shock is weakest and slowest near the central AGN and fastest in the farthest regions.

Baldi et al. (2009) assumed the unperturbed gas to be isothermal, with electron density $n_{e,gas} \propto r^{-\eta}$, where $\eta = 1.3$ was obtained by fitting the surface brightness profile in the region adiacent to the southwest arm, outside the shock. Taking a cut perpendicular to the assumed axis of the jet at distance $d = 1'.2 \simeq 5\ kpc$ they obtained the electron density profile in the direction transverse to the jet axis as $n_{e,gas} \propto (d^2 + R^2)^{-\eta/2}$, where R is the cylindrical simmetry radius. Obviously, it is therefore assumed that the jet propagates perpendicularly to the line of sight. The initial gas distribution was then made hydrostatic by imposing a static gravitational field. The shock was reproduced by depositing a large amount of energy on the simmetry axis and following the evolution with the hydrodynamical code until the shock had reached the observed size ($R \simeq 2.5\ kpc$). The projected profiles were finally determined by assuming axial symmetry and integrating along the line of sight, with the temperature scale fixed by imposing a pre-shock temperature of $kT = 0.65\ keV$.

Fig. 3.8 shows the surface brightness profile for three different simulated shocks with Mack numbers of 1.42, 1.72 and 2.04 ($\gamma = 5/3$ has been assumed for the estimate). The Mach 1.72 shock model was then chosen to compare the observed temperature profile to the simulated one. Accounting for the projected emission measure distribution, the model seems to be consistent, within the error bars, with the observations of the SW1 rim.

Baldi et al. (2009) derived from the hydrodynamical model the age of the shock (i.e. the time the shock takes to expand to the observed size) for the SW bubble, obtaining $t_{SW} \sim 2\times10^6\ yr$. Of course, the age is smaller than the ratio between the cylindrical shock radius and the present shock velocity, because in the simulation the shock strength decreases with time. Other derived parameters are the total energy which produced the shock, $E_{tot,sh} = 10^{56}$ erg, roughly equal to the estimated enthalpy, $H = 4pV = 7 \times 10^{55}\ erg$ (in the case the bubble is predominantly relativistic and expanding adiabatically; McNamara and Nulsen, 2007), and the required average mechanical power, $P_{mech} \sim 1.6 \times 10^{42}\ erg\ s^{-1}$.

The AGN hypotesis is someway strengthen by the direct observation of a X-ray point source at the center of the galaxy, coincident with the nucleus of the radio emission. The spectrum of this source is fitted by a power-law with photon-index $\Gamma = 2.5^{+0.4}_{-0.5}$ and a total luminosity of $1.6\pm0.3\times10^{38}\ erg\ s^{-1}$ in the $0.5-10\ keV$ band. This point source may be the central supermassive black hole of NGC 4636 with mass $M_{BH} \simeq 7.9 \times 10^7\ M_\odot$ (Merritt and Ferrarese, 2001).

To estimate the mass accretion rate for this supermassive black hole, Baldi et al. (2009) decided to apply the Bondi theory of steady, spherical and adiabatic accretion (Bondi, 1952). This theory requires the value for two parameters, T_∞ and n_∞, i.e. the value of temperature and density "at infinity". For practical purpose, Baldi et al. (2009) estimated these values at the Bondi accretion radius $r_{Bondi} = GM_{BH}/{c_s}^2$ ($\sim 8\ pc$ for NGC 4636) using the observed profiles. Assuming that $n \propto r^{-1}$ and normalizing at the thermal component of the spectrum in the inner $5''$ ($350\ pc$), they found $n(r_{Bondi}) \sim 5.5\ cm^{-3}$; the temperature profile was instead fitted with a second-order polynomial, obtaining $kT(r_{Bondi}) \sim 0.49\ keV$.

Using these values, the accretion rate in the Bondi model is equal to

$$\dot{M}_{Bondi} = 8.4 \times 10^{21} n\ M_8^2\ T_{0.5}^{-3/2}\ g\ s^{-1} \simeq 4.7 \times 10^{-4} M_\odot\ yr^{-1},$$

where M_8 is the mass of the supermassive black hole in units of $10^8 M_\odot$ and $T_{0.5}$ is the temperature in units of $0.5\ keV$. Assuming that at small radii this gas joins an accretion disc with typical radiative efficiency $\eta \sim 0.1$, the produced luminosity should be

$$L_{acc} = \eta \dot{M}_{Bondi} c^2 \simeq 2.7 \times 10^{42} erg\ s^{-1},$$

that is at least 4 order of magnitude greater than the observed one, suggesting a highly inefficient accretion.

3.4 The bright core

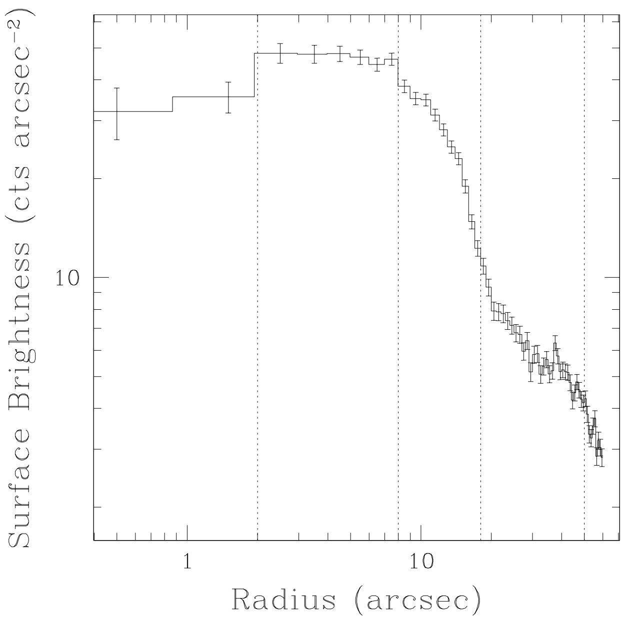

Figure 3.11: Surface brightness profile in a sector west of the galactic center ($315° - 405°$), extracted in the $0.5 - 3$ keV band. The dotted vertical lines delimitate the regions used for the spectral analysis.

As previously mentioned, NGC 4636 also shows in the X band a very bright core of ~ 1 kpc radius. Baldi et al. (2009) obtained in this region an average density of ~ 0.1 cm^{-3}, while they estimated a thermal pressure $P_{th} = 2.2\ nkT \sim 9.7 \times 10^{-11}$ $dyne\ cm^{-3}$ (assuming $n = n_p$). A finer spatial and spectral analysis has been performed, considering the emission west of the galactic center ($315° - 405°$). The surface brightness profile for this sector is plotted in Fig. 3.11, which shows a little depression at the center, a flat region for 0.14 $kpc \lesssim r \lesssim 0.56$ kpc, a sharp decline for 0.56 $kpc \lesssim r \lesssim 1.40$ kpc, while for $r \gtrsim 1.40$ kpc the surface brightness decreases with a lower slope.

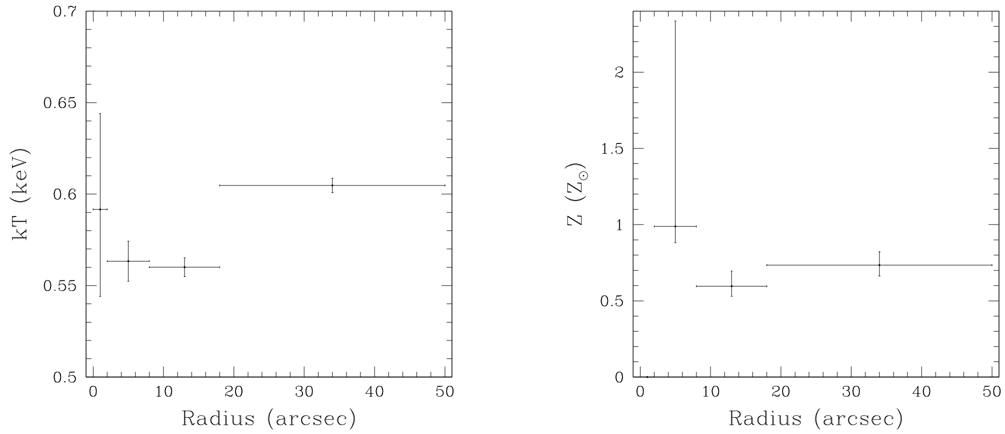

Figure 3.12: Left: projected temperature profile in the $315° - 405°$. Right: projected metal abundance profile in the $315° - 405°$.

Fig. 3.12 shows temperature and metal abundance profiles (projected quantities are plotted, because of difficulties in performing a good deprojection). The temperature is almost constant for 0.14 $kpc \lesssim r \lesssim 1.26$ kpc and it slightly increases for $r \gtrsim 1.26$ kpc. This is interesting, because the sharp decline in surface brightness at 0.56 $kpc \lesssim r \lesssim 1.40$ kpc suggests a drop in the density of a factor of at least two in this region, but this drop in the density is clearly not accompanied by a corresponding variation in the temperature. Hence, if thermal pressure is the only force acting in the central region of NGC 4636, the core is not in pressure equilibrium with the surrounding gas, being a transitory structure, expanding with $v \approx c_s$ and disappearing in $\sim R_{core}/c_s \simeq 1.5$ Myr.

Baldi et al. (2009) proposed two different explanations for the presence of a permanent bright core.

The first one involves the presence of the radio lobes linked to the x-ray cavities; in this case, the nonthermal pressure of the relativistic plasma injected by jets could secure the pressure equilibrium.

The second one considers the metal abundance gradient between the region with constant surface brightness (0.14 $kpc \lesssim r \lesssim 0.56$ kpc), with $Z = 1.0^{+1.3}_{-0.1}$ $Z_\odot$, and the adiacent region, with $Z \sim 0.6 - 0.7$ $Z_\odot$ (see Fig. 3.12). This gradient is not sufficient to balance the pressure, since the density is $\propto Z^{-1/2}$, but the error bars are large and the spectral model in the analysis should be more complex. However, Baldi et al. (2009) performed a very simple calculation of the diffusion timescale for iron and, consequently, for other metals, obtaining $t_{diff} \sim 10^{11} \div 10^{13}\ yr$ (severals order of magnitude greater than the Hubble time). So, even if there are uncertainties, the bright core could be long-lived if produced by a metal abundance gradient.

Chapter 4

Simulating AGN feedback on the X-ray hot gas in elliptical galaxies

In this chapter I will describe in detail my simulation work. In Section 4.1 and 4.2 I will discuss the gasdynamics equations that describe the evolution of hot gas in ellipticals and the adopted computational features. In Section 4.3 I will show and discuss the low resolution models, explaining how I obtained the initial conditions (4.3.1) and describing the cooling flow model (4.3.2) and several selected jet models (4.3.3). Finally, in Section 4.4, I will introduce the high resolution work, presenting the Best model found.

4.1 Gasdynamical equations

The standard set of gasdynamical equations for the evolution of the hot interstellar gas in elliptical galaxies is based on the usual conservation equations, with the addition of source and sink terms:

$$\frac{\partial \rho}{\partial t} + \nabla \cdot (\rho \mathbf{u}) = \alpha \rho_* - q \frac{\rho}{t_{cool}}, \tag{4.1}$$

$$\rho \frac{d\mathbf{u}}{dt} = \rho \left[\frac{\partial \mathbf{u}}{\partial t} + (\mathbf{u} \cdot \nabla)\mathbf{u} \right] = -\nabla P - \rho \nabla \Phi - \alpha \rho_* (\mathbf{u} - \mathbf{u}_*) \tag{4.2}$$

$$\rho \frac{d\varepsilon}{dt} - \frac{P}{\rho}\frac{d\rho}{dt} = -\frac{\rho^2 \Lambda(T)}{{m_H}^2} + \alpha \rho_* \left[\varepsilon_0 - \varepsilon - \frac{P}{\rho} + \frac{1}{2}|\mathbf{u} - \mathbf{u}_*|^2 \right] \tag{4.3}$$

where $\varepsilon = 3kT/2\mu m_H$ is the specific thermal energy.

The coefficient α is involved in all three equations as a source term describing the specific rate of gas loss from evolving stars and supernovae, i.e. $\alpha = \alpha_* + \alpha_{SN}$. The specific mass loss from stars, assuming a single burst of star formation and a Salpeter IMF, is calculated with $\alpha_*(t) = 4.7 \times 10^{-20}(t/t_n)^{-1.26}$ s^{-1} (Mathews, 1989; Brighenti and Mathews, 1999), where $t_n = 13\ Gyrs$. The term $\alpha\rho_*(\mathbf{u} - \mathbf{u}_*)$ represents a drag on the flow, assuming the gas expelled from stars has on average the mean stellar velocity $\mathbf{u}_*$, which is nonzero only in rotating galaxies. This drag term is generally negligible if the flow is subsonic. I simulated a non-rotating galaxy, so $\mathbf{u}_* = 0$ and this term has the effect of making subsonic flows even more subsonic and supersonic flows even more supersonic (Mathews and Brighenti, 2003a).

Λ in equation 4.3 is the optically thin radiative cooling function, obtained fitting the results of Sutherland and Dopita (1993).

The formation of huge central masses of cooled gas and central inflows is avoided by adding the "dropout" term $-q\rho/t_{cool}$ in equation 4.1, assuming that the cooling is spread throughout a large volume of the cooling flow (White and Sarazin, 1987; Mathews and Brighenti, 2003a). I defined the dimensionless parameter q as

$$q(T) = 2e^{-(T/T_{do})^2} \tag{4.4}$$

in order to make the removal of cooled gas significant when $T \lesssim T_{do} = 5 \times 10^5\ K$ (Gaspari et al., 2011). The local cooling time at constant pressure is assumed to be $t_{cool} = 5m_H kT/2\mu\rho\Lambda$.

4.2 Computational features

For all my numerical computations I used a two-dimensional eulerian code based on ZEUS-2D (Stone and Norman, 1992, see the Appendix;), using cylindrical coordinates R and Z. The grid is uniform up to a certain grid point in R and Z, while for the remaining part of the grid the step follows a geometric progression, $\Delta x_i = b\Delta x_{i-1}$. This choice is motivated by the need to study in detail the effects of the jet in the central region, while considering the properties of the hot gas until large radii.

4.3 Low resolution models

4.3.1 Initial conditions

I began "building" the initial conditions in order to reproduce a galaxy similar to NGC 4636. Several works show that an agreement with the observations is achieved by the inclusion of circumgalactic gas (Thomas, 1986; Bertin and Toniazzo, 1995; Brighenti and Mathews, 1998), i.e. relic hot gas who filled the halo when the massive elliptical formed near the central focus of its small group. For some large ellipticals in Virgo like NGC 4636, this ancient gas has survived after the galaxy has entered the environment of this intermediate cluster.

First of all, I tried to model the gravitational field. For stellar contribution I based my calculation on Mellier and Mathez (1987), assuming a De Vaucouleurs ($r^{1/4}$) surface brightness profile (de Vaucouleurs, 1948) with effective radius $R_e = 8.32\ kpc$ and $M_* = 4.5 \times 10^{11} M_\odot$. For the contribution of the dark matter halo I made use of a Navarro, Frenk & White profile (Navarro et al., 1996). Given the current critical density

$$\rho_c = \frac{3{H_0}^2}{8\pi G} \tag{4.5}$$

and the virial radius

$$r_{vir} = \left(\frac{3M_{vir}}{4\pi 200 \rho_c} \right)^{1/3} \tag{4.6}$$

and obtained the concentration parameter c from Fig. 4 of Bullock et al. (2001) as $c = 8.3497(1.38 M_{vir}/10^{14} M_\odot)^{-0.0911}$, the expression for M_{DM} is

$$M_{DM}(r) = M_{vir} \frac{f(r/r_s)}{f(c)}, \tag{4.7}$$

where

$$f(x) = \ln(1+x) - \frac{x}{1+x} \tag{4.8}$$

and $r_s = r_{vir}/c$ (Navarro et al., 1996; Brighenti and Mathews, 1999; Bullock et al., 2001). M_{vir} is assumed equal to $3 \times 10^{13} M_\odot$. I neglected the contribution of the hot gas, since it usually has a minimal weight in mass (see Mathews and Brighenti, 2003a; Humphrey et al., 2006).

The hot gas density is thus obtained fixing a central density $\rho_0 \simeq 8.68 \times 10^{-26}\ g\ cm^{-3}$ and a uniform temperature $T_{g,iso} = 1.05 \times 10^7\ K$ and integrating the equation of hydrostatic equilibrium in the case of spherical symmetry (see, for example, Humphrey et al., 2006)

$$\frac{dP_g}{dr} = -g(r)\rho_g$$
$$\frac{d\rho_g}{\rho_g} = -\frac{dT_g}{T_g} - \frac{\mu m_H}{kT_g} g(r)dr, \tag{4.9}$$

where, in this case, the term dT_g/T_g vanishes and $T_g \equiv T_{g,iso}$ in every grid point, since the isothermal assumption. Here $g(r)$ is the gravitational acceleration at radius r, $\mu = 0.61$ is the mean atomic weight, m_H is the atomic mass unit and k is the Boltzmann's constant.

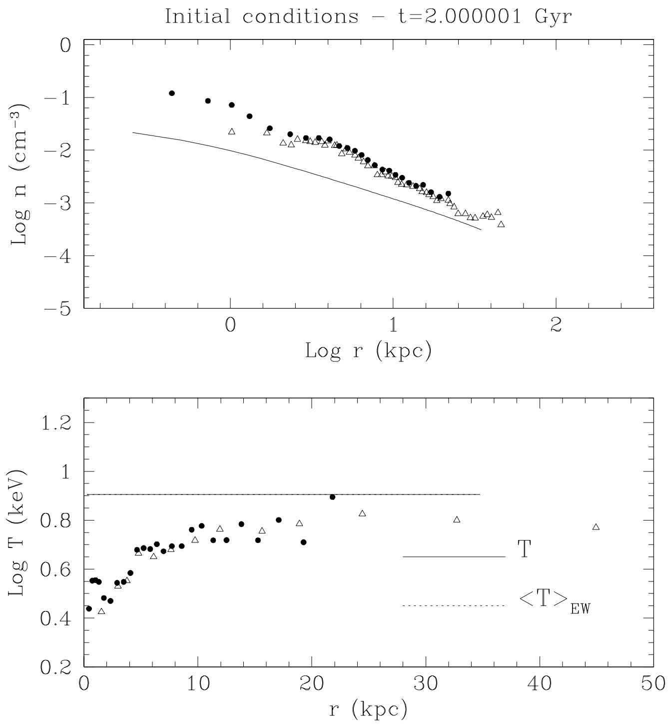

Figure 4.1: Azimuthally averaged electron number density (cm^{-3}) and temperature (keV) profiles for the initial conditions. Filled circles and open triangles are respectively Baldi et al. (2009) and Johnson et al. (2009) data.

The hydrostatic equilibrium is a good assumption, since bulk velocity and turbulent hot gas velocity are subsonic. In fact, information moving at the sound speed in the hot gas in E galaxies, $c_s = (\gamma P/\rho)^{1/2} \sim 513\ T_{keV}^{1/2}\ Km\ s^{-1}$, crosses the optical half-light radius $R_e \sim 10\ kpc$ in only $t_{sc} \sim 2 \times 10^7$

yr. If the hot gas is losing energy by radiative losses, it should flow inward at a rate $\dot{M} \sim L_{X,bol}/(5kT/2\mu m_p) \approx 1.5 M_\odot \ yr^{-1}$, where $L_{X,bol} \sim 5 \times 10^{41}$ $erg \ s^{-1}$ is a typical X-ray bolometric luminosity for massive E galaxies. Using $n_e(R_e) \sim 0.01 \ cm^{-3}$ for a typical hot gas density at R_e, the systematic inflow velocity, $u \sim \dot{M}/n_e(R_e)m_p 4\pi R_e^2 \sim 5 \ Km \ s^{-1}$, is highly subsonic, consistent with hydrostatic equilibrium. Less is known about the magnitude of turbulent motions in the hot gas, but radial velocities of diffuse optical emission lines from gas at $T \sim 10^4 \ K$ in the central regions of E galaxies (e.g., Caon et al., 2000), $v_{turb} \lesssim 150 \ Km \ s^{-1}$, suggest subsonic motion, assuming this cold gas comoves with the local hot gas.

Fig. 4.1 shows azimuthally averaged number density and temperature profiles for these initial conditions.

4.3.2 The cooling flow model

My first model is obtained evolving the initial conditions described in Section 4.3.1, according to equations 4.1, 4.2 and 4.3. I call this model "the cooling flow model", because this is what I should expect in the case of hot gas freely cooling, i.e. without any eventual additional source of heating (see Section 2.1). I evolved it for 2 Gyr, in order to use this model as initial conditions for the jet models described in Sections 4.3.4 and 4.3.5. To reach this goal, I used a low resolution 285^2 grid, with uniform step $\Delta_x = 50$ *pc* up to 10 *kpc* and with growth factor $b = 1.085$ for the geometric part, reaching ~ 460 *kpc* in each direction.

Electron number density and temperature profiles, plotted in Fig. 4.2, are reproduced satisfactorily, at least for $r \gtrsim 2.5$ *kpc*. Fig. 4.3 shows that the gas velocity is subsonic all over the domain, substaining the hydrostatic equilibrium initial assumption.

The density excess below $\simeq 2.5$ *kpc* is explained because, although the gas is in hydrostatic equilbrium, at small radii the inflow required to conserve the observed density profiles (fixing an appropriate α_*) exceeds the rate that the gas can cool, violating the assumption of steady state flow. So subsonic inflowing solutions of the sets of equations evolve toward higher densites with respect to data, until thermal conduction or any sort of central heating is introduced; in particular, AGN feedback might be able to lower the central density and modify the temperature profile.

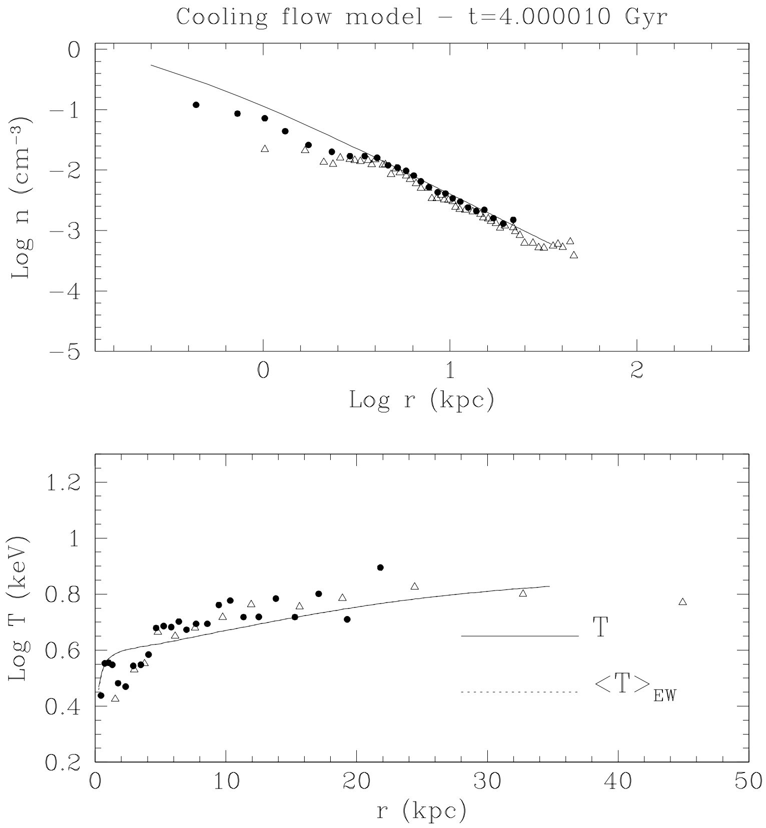

Figure 4.2: Azimuthally averaged electron number density (cm^{-3}) and temperature (keV) profiles for the simple cooling flow model. Filled circles and open triangles are respectively Baldi et al. (2009) and Johnson et al. (2009) data.

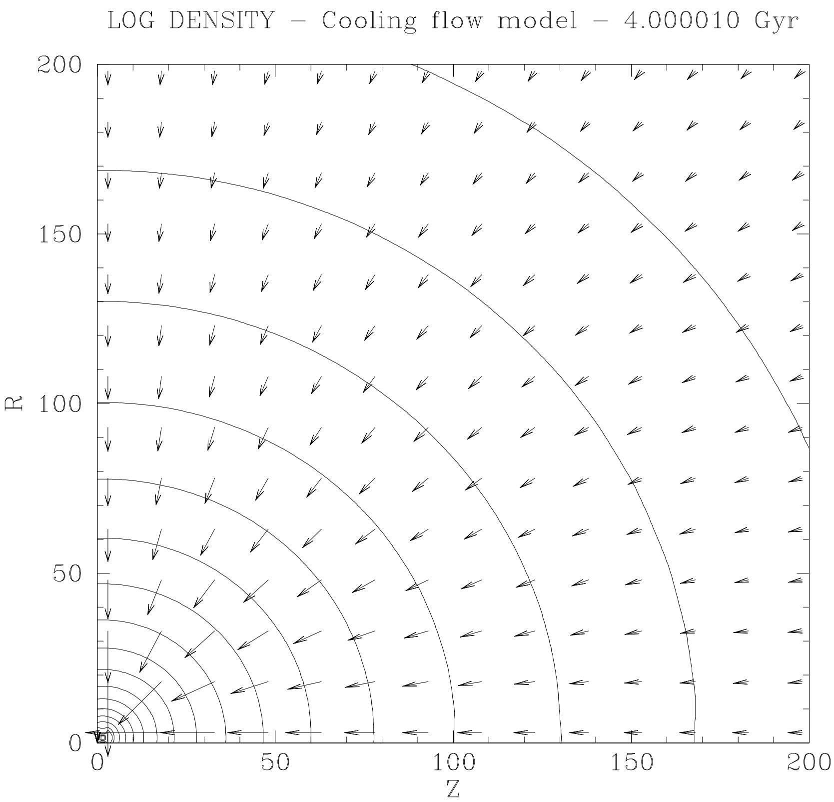

Figure 4.3: Density contour map for the "cooling flow" model. Every grid step "measures" 50 pc. Superimposed arrows show local gas velocity module and direction; a 15 grid steps long arrow represent $|\mathbf{v}| = 50\ km/s$.

4.3.3 The jet models: two different approaches

The second step was the introduction of a jet. In order to pursue this approach, I simulated two different forms of feedback:

- feedback produced by mass-loaded subrelativistic bipolar jets, with transfer of energy and momentum (subsection 4.3.4, see Gaspari et al. (2011) for observational justification of these outflows);

- feedback by a ultrarelativistic jet, creating an "artificial" cavity with energy injection at some radius (subsection 4.3.5).

So I introduced ad hoc terms in equations 4.1, 4.2 and 4.3, letting the simulation evolve for a typical timescale of 20 Myr (see Mathews and Brighenti, 2008). This timescale seemed acceptable, since the age of the shock found by Baldi et al. (2009) is $t_{sh} \sim 2 \times 10^6$ yr.

I decided to investigate the different effects of these two approaches in low resolution. So, starting from the cooling flow model output, I let the different parameters vary and tried to reproduce the observation of Baldi et al. (2009) described in Chapter 3. The used grid is the same described in Sec. 4.3.2. The low resolution gave low computational cost for each run, permitting the creation of a large set of models. In Sec. 4.3.4 and 4.3.5 I will present the most significant and interesting ones. I compared all my results particularly with the SW1 arm-like structure (see Sec. 3.2.1), which is the most studied feature in Baldi et al. (2009).

4.3.4 Mass-loaded subrelativistic jets

The mass-loaded subrelativistic jet model has been simulated by different authors in the cluster scenario (Basson and Alexander, 2003; Omma et al., 2004; Brighenti and Mathews, 2006; Sternberg and Soker, 2009; Gaspari et al., 2011).

To simulate this particular outflow, given velocity and density are set in a central cylindrical region of size indicated in Tab. 4.1.

I tested two types of "massive" jet:

- a cylindrical jet, assuming velocity uniquely directed along the z-axis;

- a conical jet, with the two components of velocity obtained fixing an "opening angle".

Figures 4.4, 4.5 and 4.6 show azimuthally averaged density and temperature profiles, the emission-weighted temperature profile in the plane $Z = 5$ kpc (that is about the distance, from the galaxy center, of the spectral

	Jet velocity (km/s)	*Density* $(10^{-25}\ g\ cm^{-3})$	*Size (pc)*
Jet p6 (cylindrical)	linear increase from 10^3 to 2×10^4	1.085	100×250
Jet p9 (cylindrical)	linear increase from 10^3 to 10^4	2.170	100×250
Jet m5 (conical, $\theta = 20°$)	linear increase from 10^3 to 8×10^3	0.217	100×250

Table 4.1: Set of parameters of 4 jets shown in Fig. 4.4, 4.5, 4.6

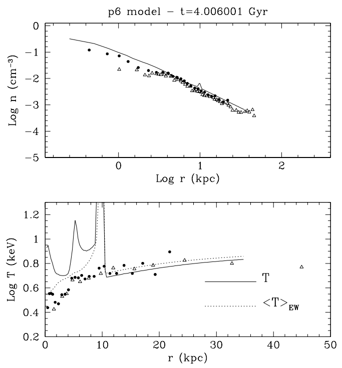

(a) n_e and T profiles

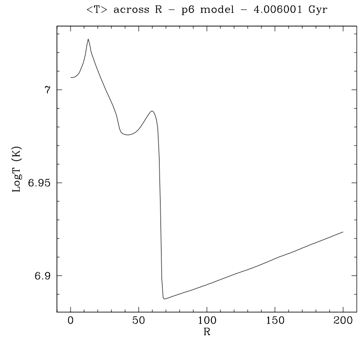

(b) Temperature jump

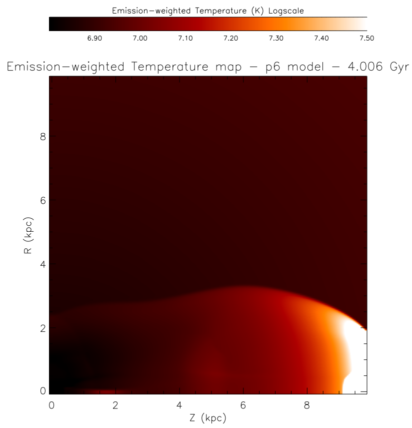

(c) Emission-weighted temperature map

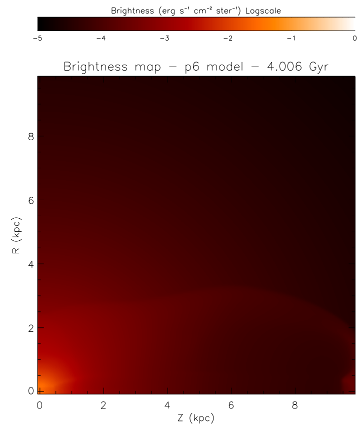

(d) Brightness map

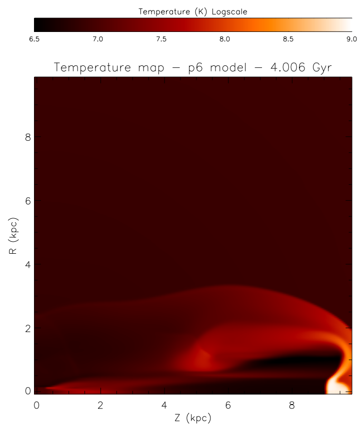

(e) Temperature map

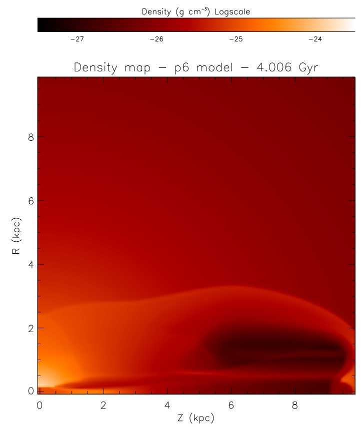

(f) Density map

Figure 4.4: Simulation results for the p6 model in Tab 4.1: (a) Electron density and temperature profiles. Filled circles and open triangles are respectively Baldi et al. (2009) and Johnson et al. (2009) data.(b) Temperature profile in the plane $Z = 5$ kpc. (c) Emission-weighted temperature map. Every value lower than $10^{6.8}$ K or greater than $10^{7.5}$ K is respectively fixed equal to this minimum or to this maximum value. (d) Brightness map. Every value lower than 10^{-5} erg s^{-1} cm^{-2} $ster^{-1}$ or greater than 1 erg s^{-1} cm^{-2} $ster^{-1}$ is respectively fixed equal to this minimum or to this maximum value. (e) Temperature map. Every value lower than $10^{6.5}$ K or greater than 10^9 K is respectively fixed equal to this minimum or to this maximum value. (f) Density map. Every value lower than $10^{-27.5}$ g cm^{-3} or greater than $10^{-23.5}$ g cm^{-3} is respectively fixed equal to this minimum or to this maximum value.

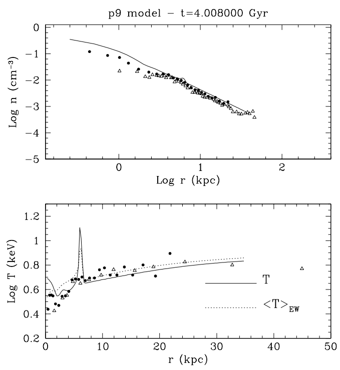

(a) n_e and T profiles

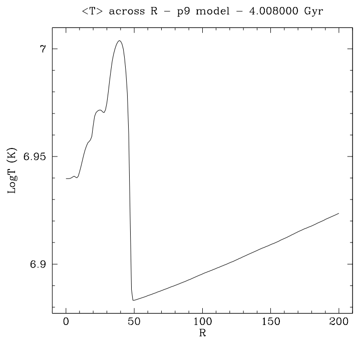

(b) Temperature jump

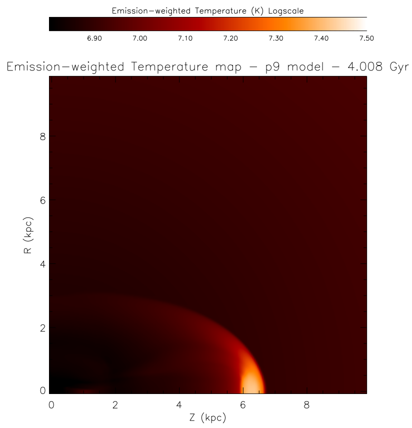

(c) Emission-weighted temperature map

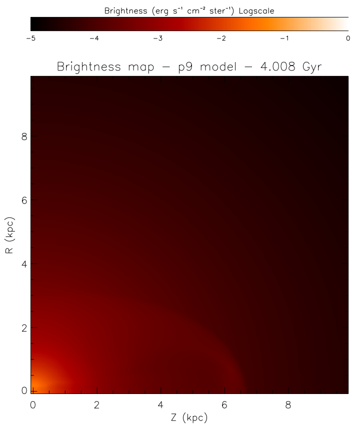

(d) Brightness map

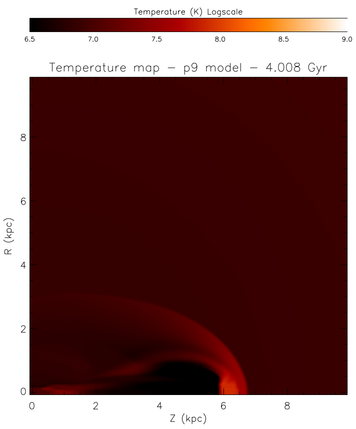

(e) Temperature map

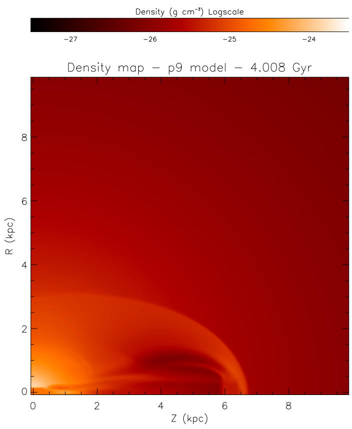

(f) Density map

Figure 4.5: Simulation results for the p9 model in Tab 4.1. (a), (b), (c), (d), (e), (f) are the same as in Fig. 4.4.

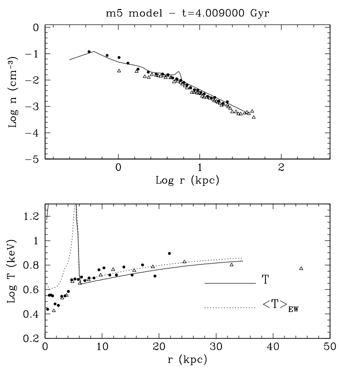

(a) n_e and T profiles

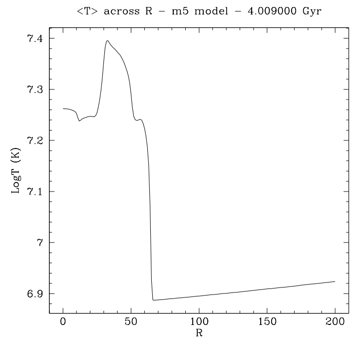

(b) Temperature jump

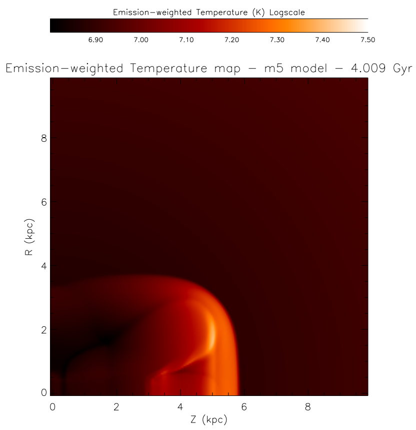

(c) Emission-weighted temperature map

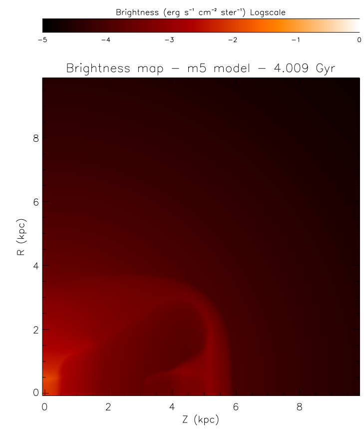

(d) Brightness map

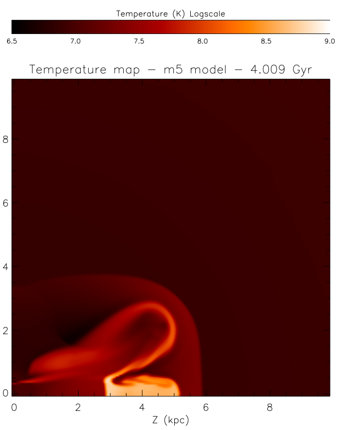

(e) Temperature map

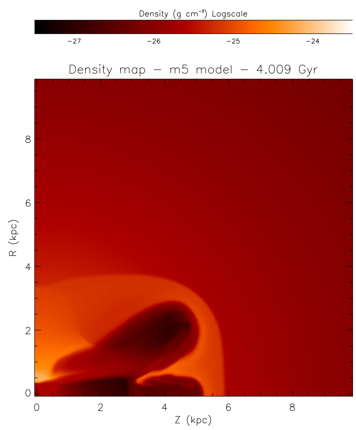

(f) Density map

Figure 4.6: Simulation results for the m5 model in Tab 4.1. (a), (b), (c), (d), (e), (f) are the same as in Fig. 4.4.

analysis region in fig 3.7 for the SW cavity observed by Baldi et al., 2009) and density, emission-weighted temperature, brightness and temperature maps for three different simulations of these massive subrelativistic jets (see Table 4.1 for their parameters). The brightness and the emission-weighted temperature are calulated using the cooling function $\Lambda(T)$ from Sutherland and Dopita (1993).

As it can be seen, none of my models is able to reproduce simultaneously all the features observed by Baldi et al. (2009). In fact, every model shows a characteristic bow-shaped external weak shock which does not depart from the galaxy center as the arm-like structure observed by Baldi et al. (2009). The azimuthally averaged (emission-weighted) temperature profile is always affected by the jet; in particular, the larger and hotter is the head of the external shock, the higher is the discrepancy with the temperature profile observed by Johnson et al. (2009) and Baldi et al. (2009). Further, every model shows a temperature excess near the center of the galaxy. Concerning the azimutally averaged density profile, it is quite well obtained only by the conical model *m5*, clearly more efficient in blowing matter to large radii. Finally, the *p6* and *p9* models produce respectively a temperature jump across the external shock of $\sim 21\%$ and $\sim 24\%$, similarly to that observed by Baldi et al. (2009), while the *m5* model produce a jump of $\sim 54\%$.

4.3.5 Cavities

Also the ultrarelativistic jet approach has been pursued by many authors in literature (see, for example, Brüggen and Kaiser, 2002; Mathews and Brighenti, 2008; Brüggen and Scannapieco, 2009).

To artificially simulate the cavity created by the head of the jet, I assumed a rate of energy injection at a fixed or time-variable position Z_{inj} on the Z-axis and then I introduced a three dimensional gaussian kernel, with standard deviation $\sigma_{inj} = 1\ kpc$, to smooth the energy injection on a three dimensional sphere.

Figures 4.7, 4.8 and 4.9 show density and temperature profiles, the emission-weighted temperature profile in the plane $Z = 5\ kpc$ and density, emission-weighted temperature, brightness and temperature maps for three different simulations of these relativistic jets (see Table 4.2 for their parameters).

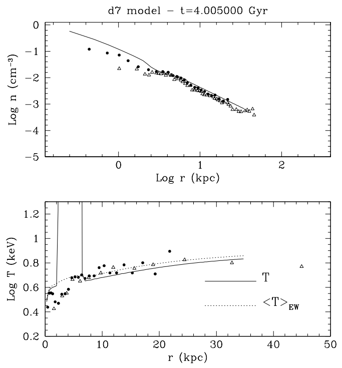

(a) n_e and T profiles

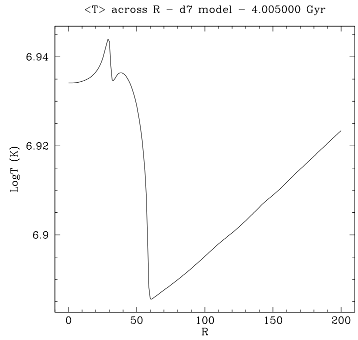

(b) Temperature jump

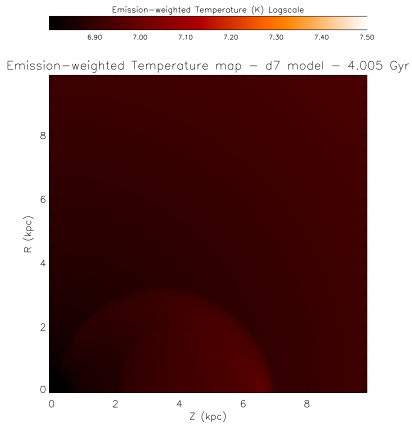

(c) Emission-weighted temperature map

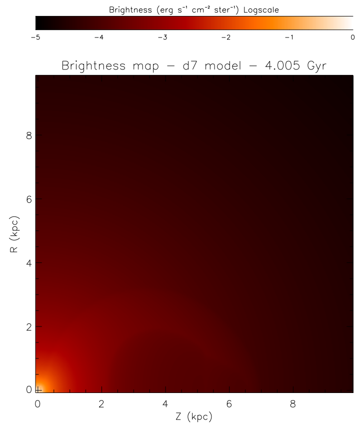

(d) Brightness map

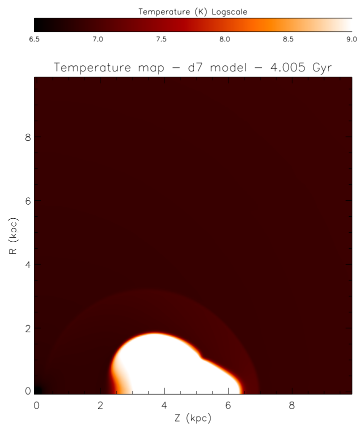

(e) Temperature map

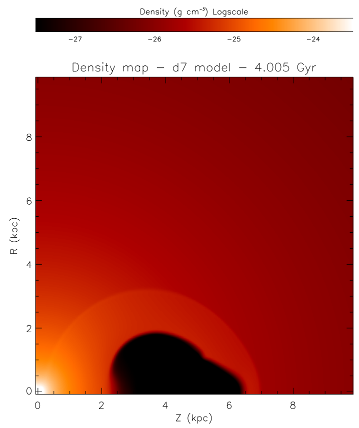

(f) Density map

Figure 4.7: Simulation results for the d7 model in Tab 4.2. (a), (b), (c), (d), (e), (f) are the same as in Fig. 4.4.

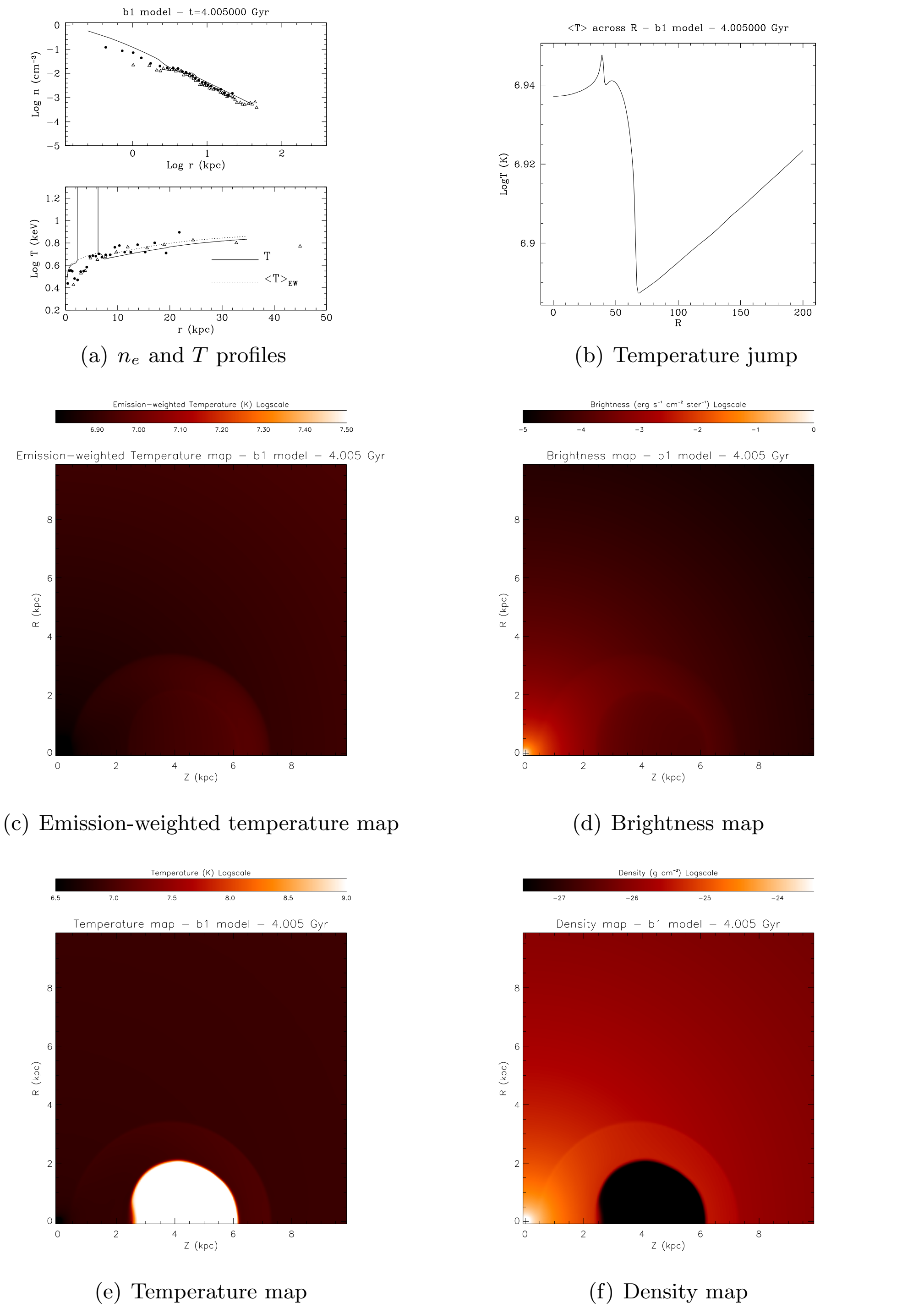

(a) n_e and T profiles

(b) Temperature jump

(c) Emission-weighted temperature map

(d) Brightness map

(e) Temperature map

(f) Density map

Figure 4.8: Simulation results for the b1 model in Tab 4.2. (a), (b), (c), (d), (e), (f) are the same as in Fig. 4.4.

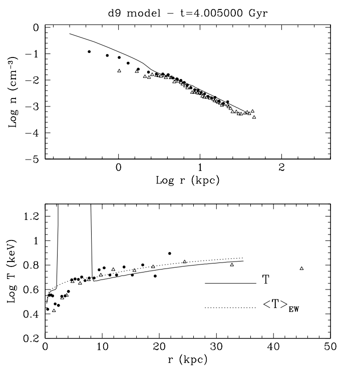

(a) n_e and T profiles

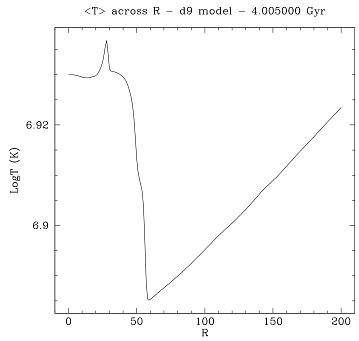

(b) Temperature jump

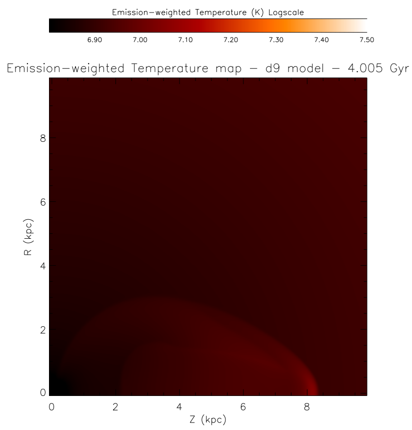

(c) Emission-weighted temperature map

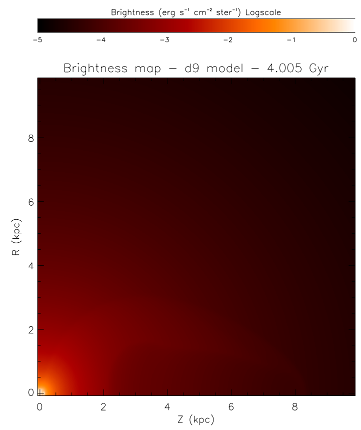

(d) Brightness map

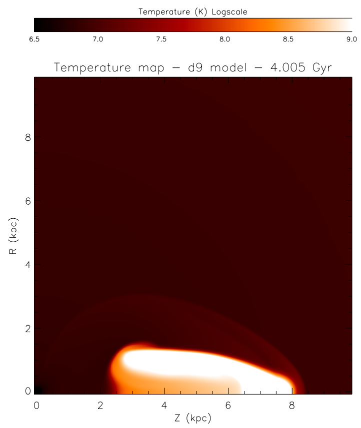

(e) Temperature map

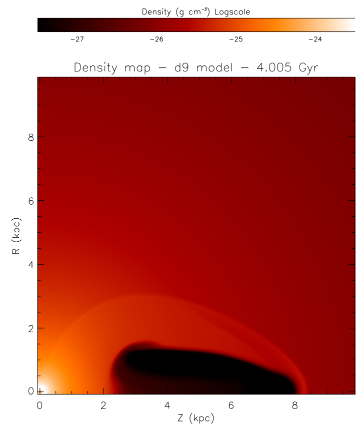

(f) Density map

Figure 4.9: Simulation results for the d9 model in Tab 4.2.(a), (b), (c), (d), (e), (f) are the same as in Fig. 4.4.

The structure of the cavity is similar to that expected for stellar winds bubbles (Weaver et al., 1977), with a quasi-spherical external shock and an internal contact discontinuity. In the *d7* and *d9* models the energy injection source is moving along the z-axis at costant velocity; this is an approximation (although admittedly rough) of the motion of the terminal working surface (i.e. the jet head) that, losing energy to create cosmic rays, should decelerate penetrating the intergalactic medium (see, for example, Guo and Mathews, 2010a). In particular, in these models, the velocity of the energy source is higher than the expansion velocity of the cavity, causing the piercing and warping of the contact discontinuity surface, but also giving the weak external shock a more elongated egg-like shape. Because of the buoyancy of the cavity, every model also shows denser and cooler shocked gas entraining the internal contact discontinuity along the jet axis; this is the "seed" of a typical feature observed in many other simulations of X-ray cavities, called "thermal jet" (Guo and Mathews, 2010b) or "cavity jet" (Mathews and Brighenti, 2008) or "drift" (Pope et al., 2010).

This "cavity" model is clearly more effective in reproducing the arm-like shape of the weak shock and the azimutally averaged (emission-weighted) temperature profiles of this simulations better match the observed ones (again with a slight temperature excess near the center of the galaxy), but the central density is still too high in every model and the temperature jumps across the shock are too small ($\sim$ 10% for all these models) with respect to the observational estimate of Baldi et al. (2009). Unfortunately, a variation of the magnitude and duration of the energy input does not give, in a reasonable time, both a significant change of the strength of the external shock and its right size.

	Energy injection rate (erg/s)	*Energy injection initial position $Z_{inj,0}$ (kpc)*	*Energy injection velocity (Km/s)*
Jet d7	8×10^{41}	3.125	~ 490
Jet b1	10^{42}	3.625	0
Jet d9	7×10^{41}	2.875	~ 880

Table 4.2: Set of parameters of 4 jets shown in Fig. 4.7, 4.8, 4.9

4.4 High resolution: the Best model

At high resolution, I used a 825^2 grid, with uniform step $\Delta_x = 20\ pc$ up to 15 kpc and with growth factor $b = 1.090$ for the geometric part, reaching ~ 260 kpc in each direction.

The simulation of a cooling flow in high resolution would have had too computational cost, so I evolved the high resolution jets in an ambient medium with temperature profile obtained fitting the observed temperature profile data; the density profile has been derived from the hydrostatic equilibrium (see eq. 4.3.1), assuming a central density $\rho_0 \simeq 2.8 \times 10^{-23}\ g\ cm^{-3}$. The choice of this temperature profile is reasonable, even if not strictly rigorous, since all the large elliptical galaxies (as NGC 4636) have similar temperature profiles and we should expect them not to dramatically effect the result of our simulations.

Bearing in mind the low resolution *p6* model, which best reproduce the structure of the observation of Baldi et al. (2009), I used its parameters ($\rho_j = 0.1085 \times 10^{-24}\ g\ cm^{-3}$ and v_j increasing linearly from 10^3 to 2×10^4 km/s) to obtain the Best (high resolution) model.

Figures 4.10, 4.11 and 4.12 show azimuthally-averaged density and temperature profiles, the emission-weighted temperature profile in the plane $Z = 5\ kpc$ (that is about the distance, from the galaxy center, of the spectral analysis region in fig 3.7 for the SW cavity observed by Baldi et al. (2009)) and density, emission-weighted temperature, brightness and temperature maps for the Best model.

The structure of the jet is very similar to that of the *p6* model, with the external weak bow-shock that is even more "arm-like". The cavity rims are instead less pronounced, since the turbulence is more developed (thanks to the higher resolution).

There is still a problem for the azimutally-averaged profiles. The central temperature is too high, but this problem can be solved by a slight different choice of the initial conditions. The emission-weighted temperature profile still has a sharp peak, at $r \simeq 10\ kpc$, caused by the jet head. We can suppose that this peak, if real, could be not observed for NGC 4636 because of a combination of the observational band selection and the instrumental off-focus limits: in fact, the jet head is very hot, so we should expect it to emit at higher energies, and the PSF and effective area of Chandra at this angular radius could give

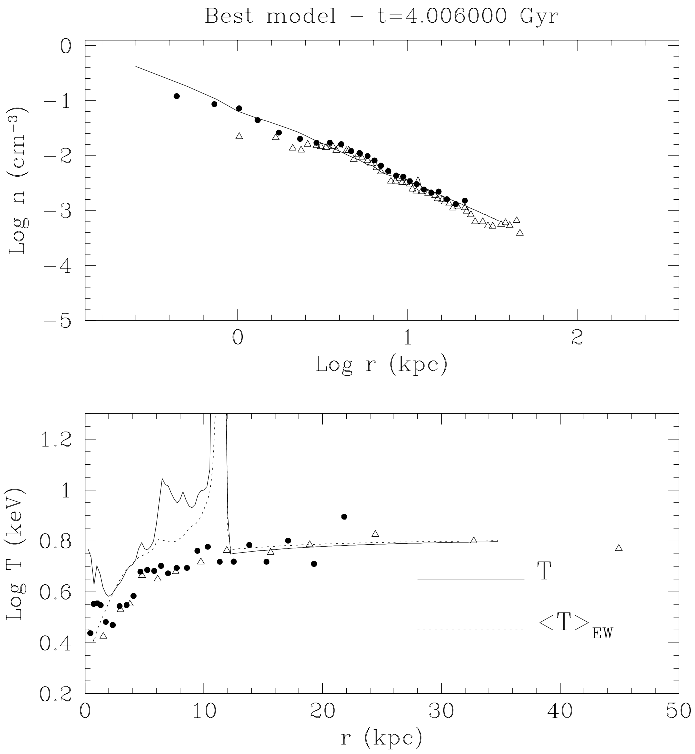

(a) n_e and T profiles

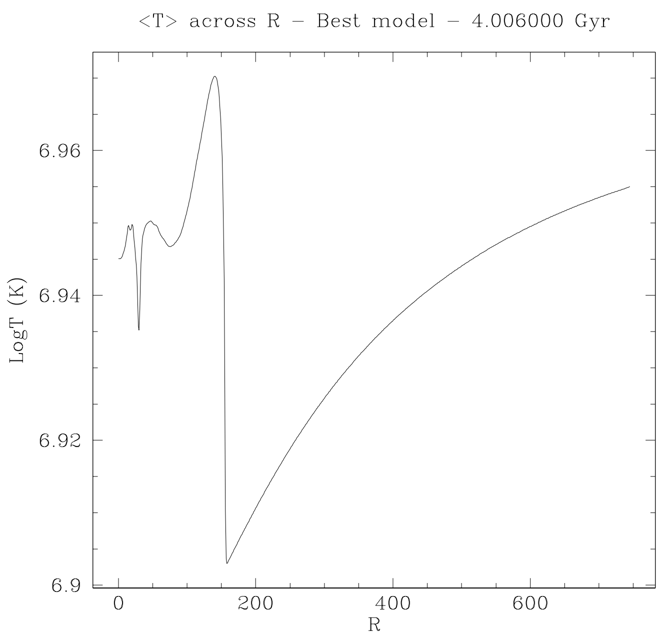

(b) Temperature jump

Figure 4.10: Simulation results for the Best model: (a) Electron density and temperature profiles. Filled circles and open triangles are respectively Baldi et al. (2009) and Johnson et al. (2009) data.(b) Temperature profile in the plane $Z = 5$ *kpc*.

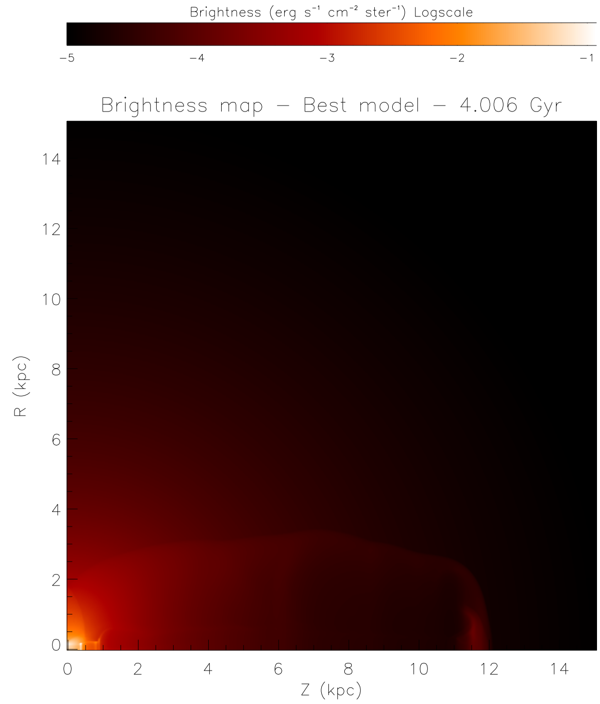

(a) Brightness map

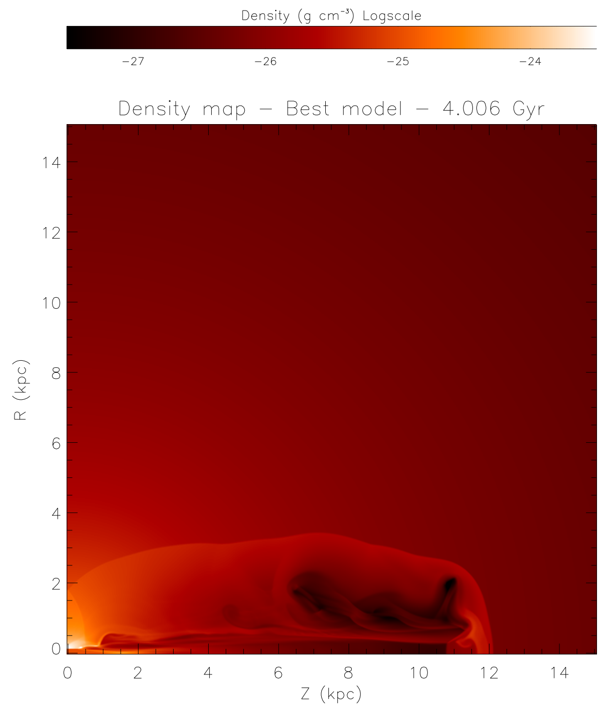

(b) Density map

Figure 4.11: Simulation results for the Best model: (a) Brightness map. Every value lower than 10^{-5} $erg\ s^{-1}\ cm^{-2}\ ster^{-1}$ or greater than 1 $erg\ s^{-1}\ cm^{-2}\ ster^{-1}$ is respectively fixed equal to this minimum or to this maximum value. (b) Density map. Every value lower than $10^{-27.5}$ $g\ cm^{-3}$ or greater than $10^{-23.5}$ $g\ cm^{-3}$ is respectively fixed equal to this minimum or to this maximum value.

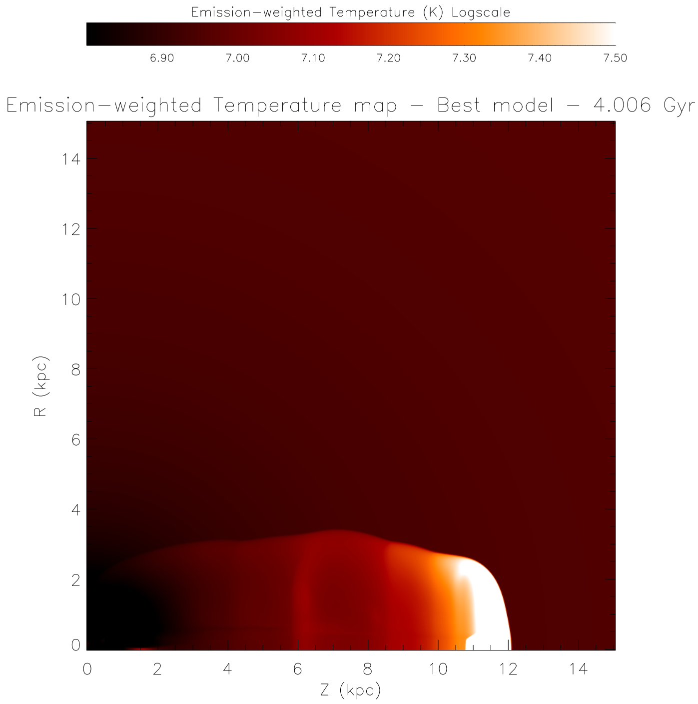

(a) Emission-weighted temperature map

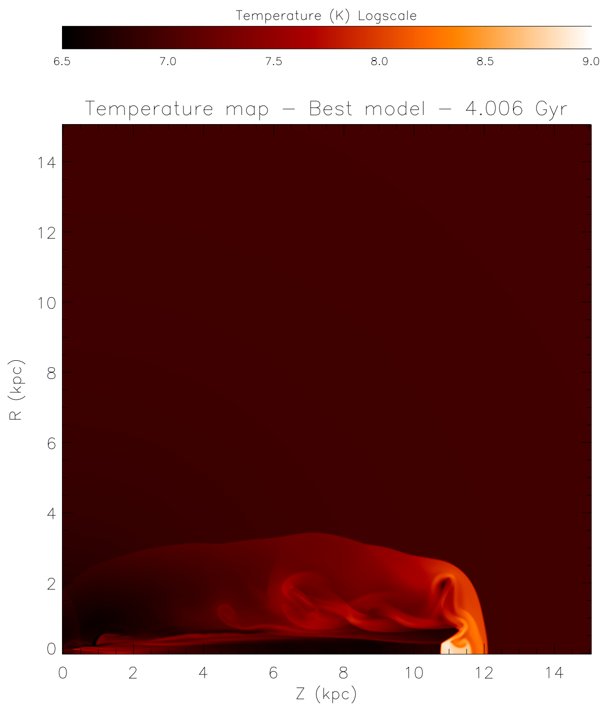

(b) Temperature map

Figure 4.12: Simulation results for the Best model: (a) Emission-weighted temperature map. Every value lower than $10^{6.8}$ K or greater than $10^{7.5}$ K is respectively fixed equal to this minimum or to this maximum value. (b) Temperature map. Every value lower than $10^{6.5}$ K or greater than 10^{9} K is respectively fixed equal to this minimum or to this maximum value.

this feature a low weight in the spectral analysis.

Finally, the temperature jump in the $Z = 5$ kpc plane is $\sim 15\%$, with temperature decreasing from ~ 0.80 keV to ~ 0.69 keV. For these pre- and post-shock temperatures there is an excess of ~ 0.05 keV with respect to the values found by Baldi et al. (2009), but this difference can be explained by the excess in the global temperature profile shown before. However, the shock has a Mach number $M \sim 1.7$, practically equal to the best value found by the simple 1-D, pressure-driven model simulated by Baldi et al. (2009). I also found that the age of shock is $t_{sh} \sim 6 \times 10^6$ yr, while that found by Baldi et al. (2009) is $\sim 2 \times 10^6$ yr.

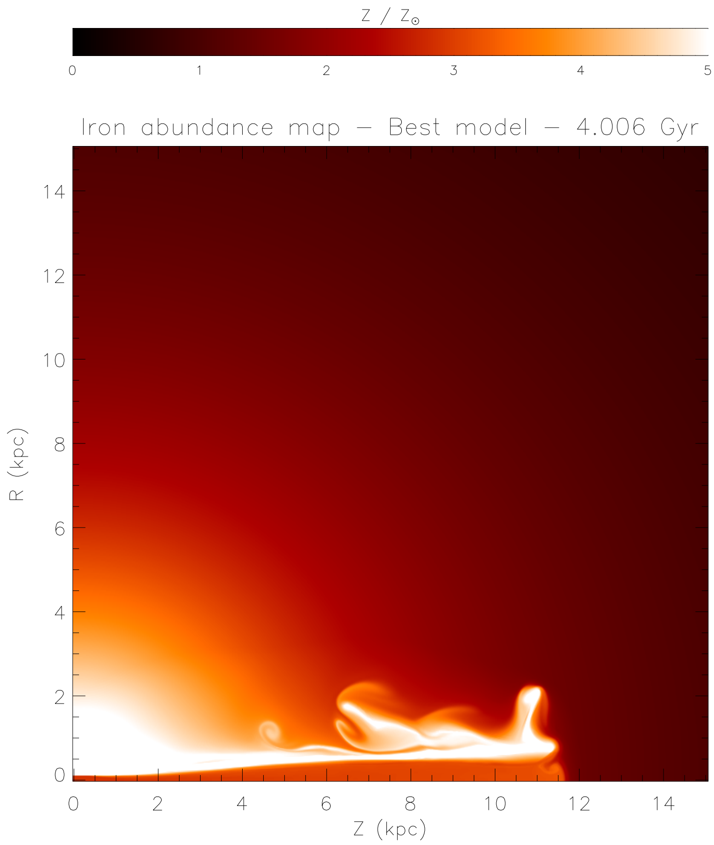

Figure 4.13: Iron abundance map (in solar abundance) for the Best model. Every value greater than 5 $Z_\odot$ is fixed equal to this maximum value.

At high resolution, I also decided to trace the evolution of the iron abundance with the presence of a jet. The intent of this further study is not quantitative, so I chose an heuristic approach to this simulation. First I assumed an initial profile of iron abundance, obtained fitting the abundance profile in Johnson et al. (2009). This choice is not rigorous at all, since I did not perform a deprojection and the central values ($Z \sim 5\ Z_{\odot}$) seem too high with respect to the general trend of iron abundance in elliptical galaxies, but it must be stressed that the aim of this research is to understand, on a quality level, how AGN outflows can spread and mix metals in the ambient gas.

The evolution of the iron abundance has been followed, in the code, with the equation (see Mathews and Brighenti, 2003a)

$$\frac{dZ_{Fe}}{dt} = (\alpha_* Z_{*,Fe} + \alpha_{SN} Z_{SN,Fe})\frac{\rho_*}{\rho_g}. \tag{4.10}$$

The iron abundance map is shown in Fig. 4.13.

It can be seen that the jet advects metal-enriched gas all along the cavity. This result is confirming both the simulative results of Pope et al. (2010) and Gaspari et al. (2011) and the observations of Kirkpatrick et al. (2009), Kirkpatrick et al. (2011) and Doria et al. (in preparation) for clusters of galaxies.

4.5 Summary

In my low resolution work I performed many different runs, testing both the mass-loaded subrelativistic jet and the relativistic jet models.

Concerning the mass-loaded jets, I concluded that conical jets, even if more efficient in depleting the central region of the galaxy, create a too much large external shock, failing in reproducing the observed "arm-like" shape. Cylindrical jets are able to create narrower external shocks (particularly in the central regions) and the choice of an increasing velocity can assure a more elongated global structure. Every model fails in reproducing the emission-weighted temperature profile, since the head of the jet, that is usually very hot, even when it is small, has a great weight in the azimuthal averaging. Anyway, this problem can be solved appealing to a combination of the observational band selection and of the instrumental off-focus limits, which can limit (or exclude at all) the contribution of the jet head in the observations.

Concerning the relativistic jets, they are surely more able to create the "arm-like" shape of the weak external shock, even if it is much more difficult to have an elongated and "opening" structure, since the typical shape of the bubble is spherical. In addition, the weak shock produced is always not enough strong to reproduce the temperature jump observed by Baldi et al. (2009).

The chosen Best model is a mass-loaded jet with $\rho_j = 1.085 \times 10^{-25}\ g\ cm^{-3}$ and v_j increasing linearly from 10^3 to $2 \times 10^4\ km/s$. The resulting temperature jump is $\sim 15\%$, consistent with the observed one, while the age of the shock is $t_{sh} \sim 6 \times 10^6\ yr$.

A study of the evolution of the iron abundance in presence of such jets has taught that metals are transported by the jet all along its axis, giving higher abundances in the formed cavity, as also confirmed by other simulative and observational works in literature.

Chapter 5

Testing the behaviour of mass-loaded jets

Throughout all the simulation work, a latere, I also tried to understand the general behaviour of the mass-loaded subrelativistic jets, especially in the galactic environment. The aim of the study was neither to treat the topic with the broadest point of view, nor to exhaust it, but only to have a better grasp of the dynamics of such jets. The adopted approach consisted, with respect to a reference model, in a huge variation of the distinctive parameters (i.e. density and velocity) of the simulated jets. In particular, I decided to keep constant either the energy flux or the momentum flux, in order to infer the relative influence of both this fundamental hydrodynamic quantities on the large- and small-scale structure of this kind of jet. Considering the clear role of space-resolution in the development of instabilities and turbulence, this study was carried on by running high-resolution simulations (the same grid parameters and initial conditions than those described in Section 4.4 were used). In the following, all the considerations that came up will be discussed.

5.1 The reference model

In order to make calculations as simple as possible, I decided to keep the jet velocity constant all over the time evolution. Then I chose as reference model the one which best resembled the Best model described in Chapter 4; this reference model has density $\rho_{j,ref} = 6.51 \times 10^{-26}\ g\ cm^{-3}$ and constant velocity $v_{j,ref} = 5000\ km\ s^{-1}$. The density map is showned in Fig. 5.1. It can be noticed that the R-width and the length of the external weak shock are similar to those of the Best model (see Fig. 4.11(b) for a comparison). Anyway, it must be stressed that, for the purposes of this study, the choice of any reference model is not unique.

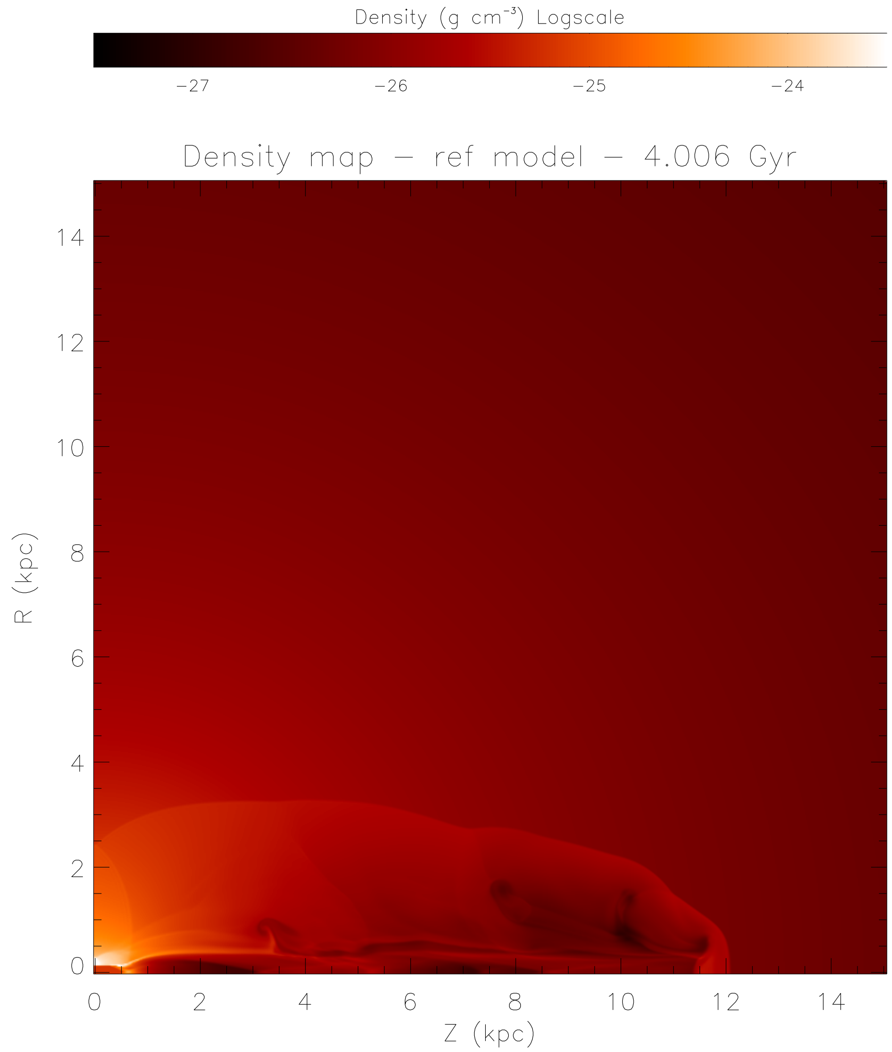

Figure 5.1: Density map for the reference model. Every value lower than $10^{-27.5}$ g cm^{-3} or greater than $10^{-23.5}$ g cm^{-3} is respectively fixed equal to this minimum or to this maximum value.

5.2 The effects of different parameters on the evolution of the jet

Starting from the reference model, I constructed two different sets of models, “p” and “e”, keeping constant, respectively, the momentum flux and the energy flux. Since the motion of the jet is unidimentional, the momentum flux is defined as the rate of momentum transfer through a surface perpendicular to the motion and it is calculated as $\rho_{j,ref} v_{j,ref}^2$, because ρ_j and v_j are constant all over the volume that defines the jet. Similarly, the energy flux is defined as the rate of energy transfer (i.e. the power) through a surface perpendicular to the motion and it is calculated as $1/2(\rho_{j,ref} v_{j,ref}^3)$. The values of momentum and energy fluxes (as defined above) for the reference model are respectively equal to $\simeq 1.63 \times 10^{-8}\ erg\ cm^{-3}$ and $\simeq 4.07\ erg\ s^{-1}\ cm^{-2}$.

So, both the "p-set" and the "e-set" were constructed respectively multiplying and dividing $v_{j,ref}$ by a factor of three and consequently adjusting the value of $\rho_{j,ref}$, as summarized in Tab. 5.1.

	Jet density	*Jet velocity*
Jet ref	$\rho_{j,ref} = 6.51 \times 10^{-26}\ g\ cm^{-3}$	$v_{j,ref} = 5 \times 10^3\ km\ s^{-1}$
Jet fp	$\rho_{j,ref}/9$	$v_{j,ref} \times 3$
Jet mp	$\rho_{j,ref} \times 9$	$v_{j,ref}/3$
Jet fe	$\rho_{j,ref}/27$	$v_{j,ref} \times 3$
Jet me	$\rho_{j,ref} \times 27$	$v_{j,ref}/3$

Table 5.1: Characteristic parameters for the reference model and the "p"and "e" sets.

Fig. 5.2 and 5.3 show the density maps for the two sets.

First of all, *fp* and *fe* models show full development of turbulence all along the length of the jet, while it is only partial for the *ref* model and totally absent in the *mp* and *me* models. This turbulence is mainly due to Kelvin-Helmoltz instability, but also Rayleigh-Taylor and Richtmyer-Meshkov instabilities are expected to play some role, even if minimal, because of the gravitational acceleration and the presence of shocks. Despite the distortion due to instabilities, in every model, the "original" contact discontinuity between the formed cavity and the contiguous shocked material is more or less visible.

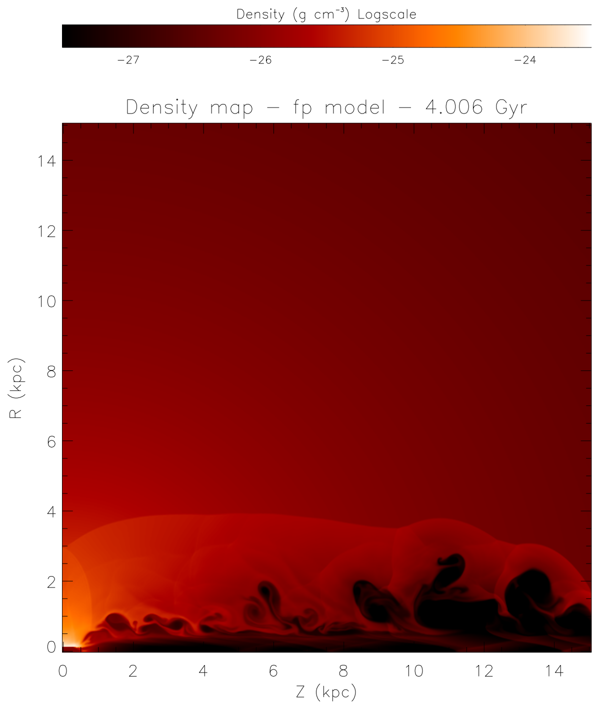

(a) *fp* model

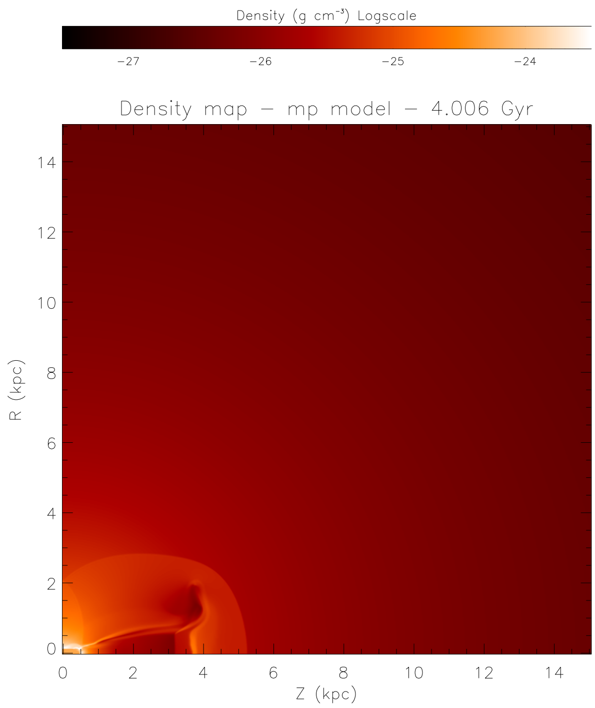

(b) *mp* model

Figure 5.2: Density maps for a) *fp* model and b) *mp* model of the "p-set". Every value lower than $10^{-27.5}$ $g\ cm^{-3}$ or greater than $10^{-23.5}$ $g\ cm^{-3}$ is respectively fixed equal to this minimum or to this maximum value.

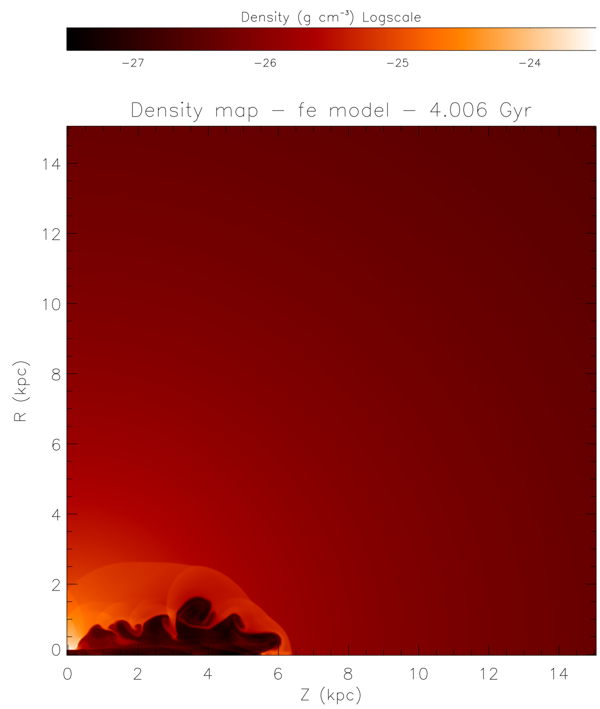

(a) *fe* model

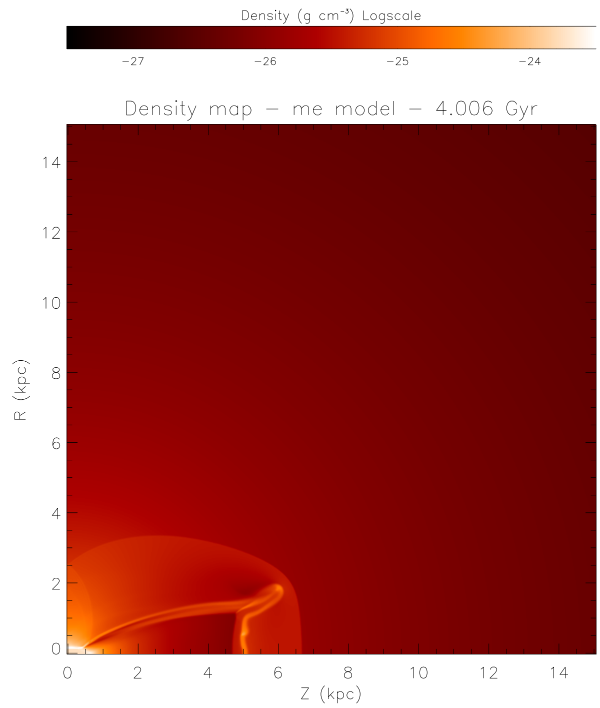

(b) *me* model

Figure 5.3: Density maps for a) *fe* model and b) *me* model of the "e-set". Every value lower than $10^{-27.5}$ $g\ cm^{-3}$ or greater than $10^{-23.5}$ $g\ cm^{-3}$ is respectively fixed equal to this minimum or to this maximum value.

Excluding the effects of turbulence, a characteristic that is common to all models (except the *fe* jet, which is the "lighter" one) is the widening of the cavity just beyond the artificial input region. This is the behaviour expected for fluids becoming supersonic after having passed a de Laval nozzle (see Blandford and Rees, 1974, for a very similar analytical model). In particular, the larger is the jet density, the wider is the contact discontinuity. This is explained knowing that the jet results to be overpressurized with respect to the external medium. In fact, for constant temperature, a higher density entails a higher pressure and, consequently, a higher expansion.

Furhtermore, *ref*, *fp* and *fe* models (which are faster) show, more or less evidently, the typical oscillation of the contact discontinuity. For these models, in fact, the cavity gas reaches the width for which it periodically expands and reconverges in attempt to match the pressure of the external gas. I might suppose that for certain velocities (much higher than the ambient sound speed), the jets reach sooner this quasi-steady configuration. In this structure is also visible the "herring-bone" structure of oblique shocks, with rarefation zones alternated with compression ones ending in a terminal Mach disk (see, for example, Clarke et al., 1986).

In conclusion, it is clear, from this study, that the evolution of these mass-loaded jets is not governed by the energy or momentum fluxes, but it is by density and velocity almost separately.

However, strangely enough, while the velocity is clearly the parameter which most regulates the jet length, the *me* jet is much less elongated than the *ref* jet. This behaviour is counterintuitive and in disagreement even with the behaviour of the jet in the *fp* model. A possible explanation is just found in the development of turbulence by Kelvin-Helmoltz instability, as described in the following section.

5.3 The Kelvin-Helmoltz instability

As already shown in Sec. 5.2, for the considered evolutionary time, the reference model shows a partial turbulence, the *fp* and *fe* models are greatly turbulent, while the *mp* and *me* models are not turbulent at all. The main physical process which drives turbulence, in the case of these jets, is the Kelvin-Helmoltz instability. Clearly, there are also other instabilities, like the Rayleigh-Taylor and the Richtmyer-Meshkov instabilities, that can potentially develop in these models and a detailed treatment of the Kelvin-Helmoltz instability should include the effects of the gravitational acceleration. In order to simplify the reasoning, I will simply treat the case of a velocity shear between the jet and the ambient gas; the following assumptions are made:

- the gravitational acceleration is negligible, since it is essentially perpendicular to the separation layer between the jet and the ambient hot gas;
- the two fluids are considered incompressible, since they are subsonic near the separation layer;
- the flow is irrotational.

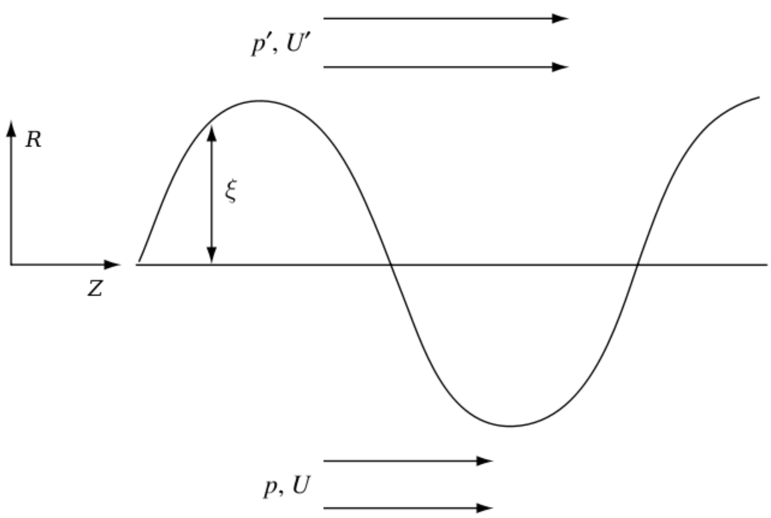

Figure 5.4: Two-dimensional configuration for the Kelvin-Helmoltz instability. The image is taken from Clarke and Carswell (2003)

The considered two-dimensional configuration is shown in Fig. 5.4 (Clarke and Carswell, 2003), with the horizontal plane $R = 0$ separating the lower and upper fluids, having respectively densities ρ and ρ' and velocities (in the Z direction) U and U'. Since the flow is irrotational, the velocity field can be described by a potential function, $\mathbf{u} = -\nabla\Phi$. The eulerian momentum equation, under the previous assumptions, is

$$-\nabla\frac{\partial\Phi}{\partial t} + \nabla\left(\frac{1}{2}u^2\right) = -\nabla\left(\frac{P}{\rho}\right). \tag{5.1}$$

This can be integrated to give

$$-\frac{\partial \Phi}{\partial t} + \left(\frac{1}{2}u^2\right) + \left(\frac{P}{\rho}\right) = F(t), \tag{5.2}$$

where $F(t)$ is a constant in space but can be a function of time. Let's consider perturbations in the surface of the interface so the perturbed position is $\xi(R,t)$. The aim is to find out if the perturbation grows, oscillates or decays with time. The velocity potential in the fluid below and above can be written as

$$\Phi = -UZ + \phi, \qquad \Phi' = -U'Z + \phi', \tag{5.3}$$

where ϕ and ϕ' are the perturbed parts, which satisfy

$$\nabla^2\phi = \nabla^2\phi' = 0 \tag{5.4}$$

as the result of the incompressibility condition $\nabla \mathbf{u} = 0$.

The velocity perturbations are caused by displacements of the interface, so the velocity potential perturbations ϕ and ϕ' must be connected with ξ. If a fluid element within the lower fluid and at the interface is taken, then its vertical velocity is given by $-\partial\phi/\partial R$. The velocity of this particular element is also given by the Lagrangian derivative of the displacement, $D\xi/Dt$. Therefore, converting the Lagrangian derivative to an eulerian one in the usual way,

$$-\frac{\partial \phi}{\partial R} = \frac{\partial \xi}{\partial t} + U\frac{\partial \xi}{\partial Z}, \qquad -\frac{\partial \phi'}{\partial R} = \frac{\partial \xi}{\partial t} + U'\frac{\partial \xi}{\partial Z} \tag{5.5}$$

at $R = 0$.

Linearising the perturbation equations, any arbitrary perturbation may be written as the sum of Fourier components, so the solutions can be written in the form

$$\xi = Ae^{i(kZ-\omega t)} \tag{5.6}$$

and ϕ and ϕ' will have the same Z and t dependences. Further, for both ϕ and ϕ' Laplace's equation (5.4) has to be satisfied and this sets the R dependence so

$$\phi = Ce^{i(kZ-\omega t)+kR}, \qquad \phi' = C'e^{i(kZ-\omega t)-kR}, \tag{5.7}$$

where the signs before the kR terms have been chosen so that the perturbations do not grow exponentially as we go far away from the separation layer. Now, substituting these solutions in 5.5,

$$i(kU - \omega)A = -kC, \qquad i(kU' - \omega)A = +kC'. \tag{5.8}$$

So there are two equations for three unknowns. To solve the system, the condition that the pressure must be continuous across the interface is assumed. Eq. 5.2 for the two fluids leads to

$$\rho\left(-\frac{\partial\phi}{\partial t} + \frac{u^2}{2}\right) = \rho'\left(-\frac{\partial\phi'}{\partial t} + \frac{u'^2}{2}\right) + K \tag{5.9}$$

at $R = 0$, with $K = \rho F(t) - \rho' F'(t)$. In principle K is a function of time, but here it is a constant because of the boundary condition that the perturbations vanish as $R \to \pm\infty$ at all times.

So, from the unperturbed values ($u = U$,$u' = U'$,$\phi = \phi' = \xi = 0$), the value of K is constrained:

$$K = \frac{1}{2}\rho U^2 - \frac{1}{2}\rho' U'^2. \tag{5.10}$$

From 5.3, u^2 and u'^2 are determined to first order,

$$\begin{aligned} u^2 &= (U\mathbf{\hat{e}_Z} - \nabla\phi)^2 = U^2 - 2U\frac{\partial\phi}{\partial Z}, \\ u'^2 &= (U'\mathbf{\hat{e}_Z} - \nabla\phi')^2 = U'^2 - 2U'\frac{\partial\phi'}{\partial Z}, \end{aligned} \tag{5.11}$$

so these, with 5.5, give

$$\rho\left(-\frac{\partial\phi}{\partial t} - U\frac{\partial\phi}{\partial Z}\right) = \rho'\left(-\frac{\partial\phi'}{\partial t} - U'\frac{\partial\phi'}{\partial Z}\right) \tag{5.12}$$

at $R = 0$. Substituting here 5.7 and then 5.8, the dispersion relation

$$\rho(kU - \omega)^2 + \rho'(kU' - \omega)^2 = 0 \tag{5.13}$$

is inferred, giving

$$\frac{\omega}{k} = \frac{\rho U + \rho' U'}{\rho + \rho'} \pm i\frac{(U - U')\sqrt{\rho\rho'}}{\rho + \rho'}. \tag{5.14}$$

In our case, $\rho = \rho_{cav}$, $\rho' = \rho_{amb}$, $U \approx v_j$ and $U' \simeq 0$, so

$$\tau_{KH} \approx \frac{1}{kv_j} \frac{\rho_{cav} + \rho_{amb}}{\sqrt{\rho_{cav}\rho_{amb}}}. \tag{5.15}$$

Near the separation layer, I assumed $\rho_{amb} = 10^{-25}\ g\ cm^{-3}$ for the upper fluid and specific values of ρ_{cav} and for the typical length scale L, that is about equal to the width of the cavity (see Tab. 5.2). Then, I used the previous formula to obtain a rough estimate of τ_{KH}. Tab. 5.2 shows the results for the *ref* model and the "e-set", confirming the general trend observed in the simulations.

	ρ_{cav} ($10^{-26}\ g\ cm^{-3}$)	L (kpc)	τ_{KH} (Myr)
Jet ref	0.32	0.50	0.57
Jet fe	0.1	0.25	0.16
Jet me	3.16	1.50	2.06

Table 5.2: Kelvin-Helmoltz instability typical timescale for the ref model and the "e-set".

The developed turbulence is useful to explain the counterintuitive length of the *fe* model. In fact, the turbulent velocity field can be thought of as being made of many eddies of differet sizes. The input energy is usually fed into the system in a way to produce the largest eddies. Kolmogorov and Oblukhov had the intuition that these large eddies feed energy to the smaller ones. On these scales, turbulence acts as a viscosity, leading to a dissipation of energy in the smallest eddies, where the kinetic energy of the jet is converted into heat (Landau and Lifshitz, 1959; Choudhuri, 1998).

Conclusions

My work consisted in simulating the interaction between a jet and the ambient hot gas in elliptical galaxies. I used a two-dimensional eulerian code based on ZEUS-2D (Stone and Norman, 1992) and assuming cylindrical symmetry with respect to the jet axis.

In particular, I decided to start from the X-ray observation with the Chandra satellite of NGC 4636, in the recent paper of Baldi et al. (2009), trying to establish whether it is possible to reproduce the properties of the observed bright structures.

At low resolution, I first simulated a classical cooling flow and then I tried to model the effect of a jet, adopting two different approaches frequently used in literature. The first one consists in simulating mass-loaded subrelativistic jets, with transfer of energy and momentum (see, for example, Basson and Alexander, 2003; Omma et al., 2004; Brighenti and Mathews, 2006; Sternberg and Soker, 2009; Gaspari et al., 2011), setting typical density and velocity in a cylindrical region at the origin of the axes. The second one consists in simulating an “artificial” cavity created and fed by the head of a relativistic jet (see, for example, Brüggen and Kaiser, 2002; Mathews and Brighenti, 2008; Brüggen and Scannapieco, 2009): in this case I fixed a energy input at a certain distance from the galactic center. The low computational cost of low resolution runs has been useful to seek and find the best values of the characteristic parameters.

Concerning the mass-loaded jets, I concluded that conical jets, even if more efficient in depleting the central region of the galaxy, create a too much large external shock, failing in reproducing the observed “arm-like” shape. Cylindrical jets are able to create narrower external shocks (particularly in the central regions) and the choice of an increasing velocity can assure a more elongated global structure. Every model fails in reproducing the emission-weighted temperature profile, since the head of the jet, that is usually very hot, even when it is small, has a great weight in the azimuthal averaging. Anyway, this problem can be solved appealing to a combination of the observational band selection and of the instrumental off-focus limits, which can limit (or exclude at all) the contribution of the jet head in the observations.

Concerning the relativistic jets, they are surely more able to create the "arm-like" shape of the weak external shock, even if it is much more difficult to have and elongated and "opening" structure, since the typical shape of the bubble is spherical. In addition, the weak shock produced is always not enough strong to reproduce the temperature jump observed by Baldi et al. (2009).

At high resolution, I hence decided to focus on the mass-loaded jet model, more effective in the comparing with the observations and clearly more "physical" in describing the whole dynamics of the jet and the heating process. The chosen Best model is a jet with $\rho_j = 0.1085 \times 10^{-24}\ g\ cm^{-3}$ and v_j increasing linearly from 10^3 to $2 \times 10^4\ km/s$. The external weak bow is enough similar to the observed "arm-like" structures and the resulting temperature jump is $\sim 15\%$, consistent with the observed one.

A study of the evolution of the iron abundance in presence of such jets has taught that metals are transported by the jet all along its axis, giving higher abundancies in the formed cavity, as also confirmed by other simulative and observational works in literature (Pope et al., 2010; Gaspari et al., 2011; Kirkpatrick et al., 2009, 2011).

Finally, I also tried to understand the general behaviour of the mass-loaded subrelativistic jets, especially in the galactic environment. The adopted approach consisted, with respect to a reference model, in a huge variation of the distinctive parameters (i.e. density and velocity) of the simulated jets. In particular, I decided to keep constant either the energy flux or the momentum flux, in order to infer the relative influence of both this fundamental hydrodynamic quantities on the large- and small-scale structure of this kind of jet. Considering the clear role of space-resolution in the development of instabilities and turbulence, this study was carried by running high-resolution simulations. The first conclusion is that the evolution of the jets is not dramatically influenced neither by the momentum flux, nor by the energy flux, but it is, almost independently, by the density and the velocity. Furthermore, when the Kelvin-Helmoltz instability develops enough turbulence, this turbulence is able to steal kinetic energy from the jet (progressively "feeding" the smallest eddies), converting it into thermal energy.

Appendix

For all the simulations, I used a two-dymensional eulerian code. Its structure is fundamentally that of ZEUS-2D (Stone and Norman, 1992). In this Appendix I will introduce the fundamental peculiarities of this code.

The grid

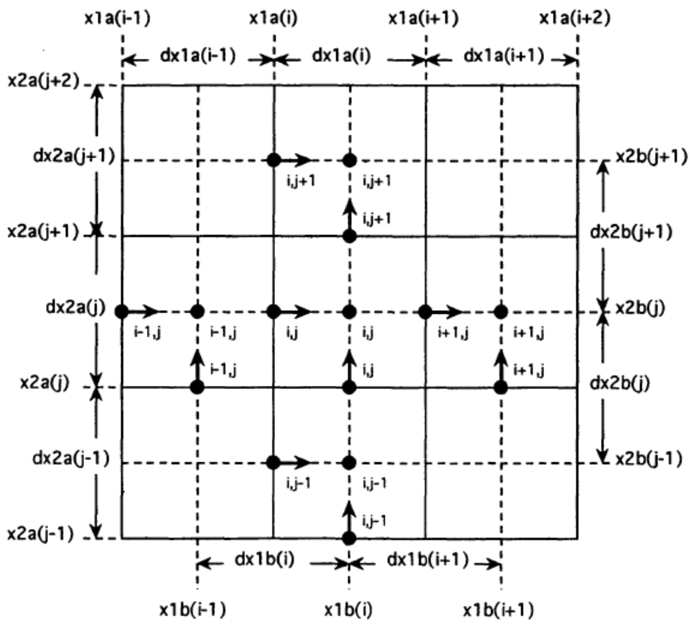

Figure A.1: Spatial positions of an arbitrary point in the two-dimensional staggered mesh. The "a-mesh" values are located at zone edges (solid lines), while the "b-mesh" values are located at zone centers. Figure taken from Stone and Norman (1992).

The code solves the hyperbolic hydrodynamical PDEs with the finite-difference method, which involves a grid on which variables are discretized. The two indipendent coordinates directions are labeled as x_1 and x_2. The number of grid points of this mesh is free and, at each boundary, two rows of "ghost" zones are added in order to specify the boundary conditions. While it is assumed only two spatial dimensions, no restriction is made on the components of the vector or tensor variables (such as velocity), that are evolved as functions of the two spatial coordinates. This formulation is often called 2.5-dymensional dynamics, and it is essential for self-consistent simulations of rotating flows and for the proper treatment of all possible wave modes in MHD.

The peculiarity of the code is the use of a staggered mesh, with a "a-mesh" and a "b-mesh" (see Fig. A.1) so that scalars and the individual components of vectors and tensors are centered at different locations on the mesh. There are two advantages for this choice. The first is that, for example, vectors which are formed from differencing scalars are in a centered location between these scalars and centered differencies are second-order accurate (while forward and backward differencies have first-order accuracy). The second is that a staggered mesh reduces the number of interpolation needed for solving the advection equations in the Transport Step (see later), with the velocities, when centered on zone interfaces, naturally describe the flux of fluid into or out of that zone.

The covariant formalism

The covariant formalism is used to write the equations in a coordinate-independent way. For orthogonal coordinate systems, like those used in the code, the metric tensor can be written as

$$g_{ij} = \begin{pmatrix} h_1^2 & 0 & 0 \\ 0 & h_2^2 & 0 \\ 0 & 0 & h_3^2 \end{pmatrix}.$$

For carthesian coordinates

$$(x_1, x_2, x_3) = (x, y, z); \qquad (h_1, h_2, h_3) = (1, 1, 1).$$

For cylindrical coordinates

$$(x_1, x_2, x_3) = (Z, R, \phi); \qquad (h_1, h_2, h_3) = (1, 1, R).$$

For spherical polar coordinates

$$(x_1, x_2, x_3) = (r, \theta, \varphi); \qquad (h_1, h_2, h_3) = (1, r, r\sin\theta).$$

In this two-dimensional case, x_3 is ignored and

$$h_1 = 1 = g_1,$$

$$h_2 = f(x_1) = g_2,$$

$$h_3 = f(x_1)f(x_2) = g_2 g_3.$$

Without loss of generality, g_1 is dropped from the difference equations and each scale factor is coherently defined on both the “a” and “b” meshes, since they are functions of the coordinates. Their derivatives are, for carthesian coordinates,

$$\frac{\partial g_2}{\partial x_1} = 0, \qquad \frac{\partial g_3}{\partial x_2} = 0,$$

for cylindrical coordinates

$$\frac{\partial g_2}{\partial x_1} = 0, \qquad \frac{\partial g_3}{\partial x_2} = 1,$$

for spherical polar coordinates

$$\frac{\partial g_2}{\partial x_1} = 1, \qquad \frac{\partial g_3}{\partial x_2} = \cos\theta.$$

The volume difference formulae are used whenever necessary, so also volume factors are defined. For carthesian coordinates,

$$dvl1 = \Delta x, \qquad dvl2 = \Delta y,$$

for cylindrical coordinates

$$dvl1 = \Delta Z, \qquad dvl2 = \Delta(R^2/2),$$

for spherical polar coordinates

$$dvl1 = \Delta(r^3/3), \qquad dvl2 = \Delta(-\cos\theta).$$

Splitting the equations: Source and Transport Steps

In this section I will describe the numerical solution of the hydrodynamical equations, written with the previously mentioned covariant formalism. I will avoid going into the details, for they can be found on Stone and Norman (1992). Most interestingly, the implementation of equations is based on the splitting of the operators. This method breaks the solution of the PDEs into parts, with each part representing a single term in the equations, evaluating it successively and using the results from the update preceding it. For example, the dynamical equations can be written schematically as

$$\frac{\partial y}{\partial t} = \mathscr{L}(y).$$

Assuming the operator $\mathscr{L}(y)$ can be split into parts, $\mathscr{L}(y) = \mathscr{L}_1(y) + \mathscr{L}_2(y) + ...$, then the operator split solution procedure is

$$(y^1 - y^0)/\Delta t = L_1(y^0),$$

$$(y^2 - y^1)/\Delta t = L_2(y^1),$$

$$(y^3 - y^2)/\Delta t = ...,$$

where the L_i are finite-difference representations of the corresponding operators $\mathscr{L}_i$.

The individual parts in the solution procedure are grouped in two steps, called the Source and the Transport steps. The latter accounts for the fluid advection part of the equations by solving it in integral form, the former solve in differential form the remaining source and sink terms.

Another noteworthy characteristic of this code is the introduction, in the Source step, of an artificial viscosity, by adding ad hoc "viscous pressure" terms to the equations. The artificial viscosity acts to smooth discontinuities which may appear in the flow, where the finite-difference equations break down. A non linear viscous pressure, sensitive only to compression, is chosen, since it can give the correct entropy jump across shocks and the correct shock propagation velocity, while having negligible effect away from shocks. The used approach involves the analysis of planar shocks in one dimension, then extending the coefficients of viscosity in each direction independently and using them to compute separtae scalar artificial pressures for the update in each direction.

Last but not least, I want to briefly explain the approach used to solve the integral equations in the Transport step. The finite-difference approximation makes use of the fluxes of every quantity q onto the faces of the volume of a zone centered on q (control volume). This is particularly simple thanks to the introduction of the staggered mesh, having the velocities naturally centered at the faces of the control volume. The advection is usually simplified by using directional splitting and it is achieved making use of the Upwind method. Upwindedness dictates that the chosen interface values should be that given by the distribution of the variable upstream of the interface. So, such distribution is represented with different accuracy, according to the order of the interpolation polynomials. In particular, the code permits the use of a *Donor cell* first-order method, assuming the variable q is constant with a zone, a *van Leer* second-order method, using a piecwise linear function, and a *PPA* (piecewise parabolic advection) third-order scheme, using a a parabolic interpolation onto a five-point "molecule" centered on the zone being updated.

Boundary conditions

In the code, several different boundary conditions are implemented, which can be applied depending on the geometry and physics of the problem being solved:

- Reflecting Boundary Condition: All zone-centered variables and the tangential components of velocity in the ghost zones are set equal to the corresponding values of their images among active zones. The normal component of velocity is set to zero on the boundary and reflected for the second ghost zone.

- Axis of Symmetry Boundary Condition: This condition is identical to the reflecting boundary condition, except that the zone-centered 3-component of velocity is set equal to the negative of the value in the corresponding active zones, forcing it to go to zero on the boundary.

- Inflow Boundary Condition: Here the values of all the variables in the ghost zones are held equal to a set of predetermined values (which may be allowed to vary in time). Outflow is not permitted.

- Outflow Boundary Condition: All the values of variables in the ghost zones are set equal to the values in the corresponding active zones (extrapolated the flow beyond the boundary).

- Periodic Boundary Condition: All zone-centered variables and the tangential components of velocity in the ghost zones are set equal to the values in the corresponding active zones on the other side of the grid. The normal component of velocity in the second ghost zone is set equal to the value in the appropriate active zone on the opposite side of the grid, while on the boundary it is computed from the difference equations.

Stability: choosing the time step

The time step is chosen in order to satisfy the Courant-Friedrichs-Lewy (CFL) stability condition. Physically, this condition can be understood as imposing the distance that information can travel in one time step to be smaller than one spatial grid zone. For multidimensional flows, a suitable time step is the smallest among those derived from the CFL condition in each orthogonal direction.

In particular, in this code

$$\Delta t = C_0/[\max(\delta t_1^{-2} + \delta t_2^{-2} + \delta t_3^{-2} + \delta t_4^{-2})]^{1/2},$$

where the maximum is taken over all zones, C_0 is the Courant number, typically ≈ 0.5) and

$$\delta t_1 = [\min(\Delta x_1, \Delta x_2)]/C_a$$

(C_a is the local adiabatic speed of sound),

$$\delta t_2 = \Delta x_1/(v_1 - vg_1), \qquad \delta t_3 = \Delta x_2/(v_2 - vg_2)$$

(vg is the grid velocity)

and δt_4 arises from the inclusion of the artificial viscosity, with typical length scale l (describing the "strength" of the viscosity), leading to

$$\delta t_4 = \min\left(\frac{(\Delta x_1)^2}{4l^2(\Delta v_1/\Delta x_1)}, \frac{(\Delta x_2)^2}{4l^2(\Delta v_2/\Delta x_2)}\right).$$

Bibliography

S. W. Allen, A. C. Fabian, A. C. Edge, M. W. Bautz, A. Furuzawa, and Y. Tawara. ASCA and ROSAT observations of distant, massive cooling flows. MNRAS, 283:263–281, 1996.

S. W. Allen, G. B. Taylor, P. E. J. Nulsen, R. M. Johnstone, L. P. David, S. Ettori, A. C. Fabian, W. Forman, C. Jones, and B. McNamara. Chandra X-ray observations of the 3C 295 cluster core. MNRAS, 324:842–858, 2001.

A. Baldi, W. Forman, C. Jones, R. Kraft, P. Nulsen, E. Churazov, L. David, and S. Giacintucci. The Unusual X-Ray Morphology of NGC 4636 Revealed by Deep Chandra Observations: Cavities and Shocks Created by Past Active Galactic Nucleus Outbursts. ApJ, 707:1034–1043, 2009.

J. F. Basson and P. Alexander. The long-term effect of radio sources on the intracluster medium. MNRAS, 339:353–359, 2003.

M. C. Begelman and A. C. Fabian. Turbulent mixing layers in the interstellar and intracluster medium. MNRAS, 244:26P–29P, 1990.

G. Bertin and T. Toniazzo. Cooling Flow Models of the X-Ray Emission and Temperature Profiles for a Sample of Elliptical Galaxies. ApJ, 451:111–+, 1995.

E. Bertschinger. Self-similar secondary infall and accretion in an Einstein-de Sitter universe. ApJS, 58:39–65, 1985.

Y. Birnboim and A. Dekel. Virial shocks in galactic haloes? MNRAS, 345: 349–364, 2003.

R. D. Blandford and M. J. Rees. A 'twin-exhaust' model for double radio sources. MNRAS, 169:395–415, 1974.

H. Böhringer, E. Belsole, J. Kennea, K. Matsushita, S. Molendi, D. M. Worrall, R. F. Mushotzky, M. Ehle, M. Guainazzi, I. Sakelliou, G. Stewart, W. T. Vestrand, and S. Dos Santos. XMM-Newton observations of M 87 and its X-ray halo. A&A, 365:L181–L187, 2001.

H. Bondi. On spherically symmetrical accretion. MNRAS, 112:195–+, 1952.

R. G. Bower, I. G. McCarthy, and A. J. Benson. The flip side of galaxy formation: a combined model of galaxy formation and cluster heating. MNRAS, 390:1399–1410, 2008.

F. Brighenti and W. G. Mathews. Stopping Cooling Flows with Jets. ApJ, 643:120–127, 2006.

F. Brighenti and W. G. Mathews. X-Ray Observations and the Structure of Elliptical Galaxies. ApJ, 486:L83+, 1997.

F. Brighenti and W. G. Mathews. Recent X-Ray Observations and the Evolution of Hot Gas in Elliptical Galaxies: Evidence for Circumgalactic Gas. ApJ, 495:239–+, 1998.

F. Brighenti and W. G. Mathews. Evolution of Hot Gas and Dark Halos in Group-dominant Elliptical Galaxies: Influence of Cosmic Inflow. ApJ, 512: 65–78, 1999.

B. A. Brown and J. N. Bregman. Emission Mechanisms in X-Ray-faint Galaxies. ApJ, 547:154–161, 2001.

M. Brüggen and C. R. Kaiser. Hot bubbles from active galactic nuclei as a heat source in cooling-flow clusters. Nature, 418:301–303, 2002.

M. Brüggen and E. Scannapieco. Self-regulation of active galactic nuclei in galaxy clusters. MNRAS, 398:548–560, 2009.

J. S. Bullock, T. S. Kolatt, Y. Sigad, R. S. Somerville, A. V. Kravtsov, A. A. Klypin, J. R. Primack, and A. Dekel. Profiles of dark haloes: evolution, scatter and environment. MNRAS, 321:559–575, 2001.

D. A. Buote. Oxygen Absorption in Cooling Flows. ApJ, 532:L113–L116, 2000a.

D. A. Buote. ROSAT Evidence for Intrinsic Oxygen Absorption in Cooling Flow Galaxies and Groups. ApJ, 544:242–257, 2000b.

D. A. Buote. Oxygen Absorption in M87: Evidence for a Warm+Hot Interstellar Medium. ApJ, 548:652–670, 2001.

D. A. Buote, C. R. Canizares, and A. C. Fabian. X-ray emission lines and multiphase gas in elliptical galaxies and galaxy clusters. MNRAS, 310:483–510, 1999.

D. A. Buote, A. D. Lewis, F. Brighenti, and W. G. Mathews. XMM-Newton and Chandra Observations of the Galaxy Group NGC 5044. II. Metal Abundances and Supernova Fraction. ApJ, 595:151–166, 2003a.

D. A. Buote, A. D. Lewis, F. Brighenti, and W. G. Mathews. XMM-Newton and Chandra Observations of the Galaxy Group NGC 5044. I. Evidence for Limited Multiphase Hot Gas. ApJ, 594:741–757, 2003b.

D. A. Buote, F. Brighenti, and W. G. Mathews. Ultralow Iron Abundances in the Distant Hot Gas in Galaxy Groups. ApJ, 607:L91–L94, 2004.

C. R. Canizares, G. Fabbiano, and G. Trinchieri. Properties of the X-ray emitting gas in early-type galaxies. ApJ, 312:503–513, 1987.

N. Caon, D. Macchetto, and M. Pastoriza. A Survey of the Interstellar Medium in Early-Type Galaxies. III. Stellar and Gas Kinematics. ApJS, 127:39–58, 2000.

D. Chakrabarty and S. Raychaudhury. The Distribution of Dark Matter in the Halo of the Early-Type Galaxy NGC 4636. AJ, 135:2350–2357, 2008.

A. R. Choudhuri. *The physics of fluids and plasmas : an introduction for astrophysicists*. Cambridge University Press, 1998.

E. Churazov, M. Brüggen, C. R. Kaiser, H. Böhringer, and W. Forman. Evolution of Buoyant Bubbles in M87. ApJ, 554:261–273, 2001.

E. Churazov, W. Forman, A. Vikhlinin, S. Tremaine, O. Gerhard, and C. Jones. Measuring the non-thermal pressure in early-type galaxy atmospheres: a comparison of X-ray and optical potential profiles in M87 and NGC 1399. MNRAS, 388:1062–1078, 2008.

L. Ciotti, A. D'Ercole, S. Pellegrini, and A. Renzini. Winds, outflows, and inflows in X-ray elliptical galaxies. ApJ, 376:380–403, 1991.

C. J. Clarke and R. F. Carswell. *Principles of Astrophysical Fluid Dynamics*. Cambridge University Press, 2003.

D. A. Clarke, M. L. Norman, and J. O. Burns. Numerical simulations of a magnetically confined jet. ApJ, 311:L63–L67, 1986.

D. J. Croton, V. Springel, S. D. M. White, G. De Lucia, C. S. Frenk, L. Gao, A. Jenkins, G. Kauffmann, J. F. Navarro, and N. Yoshida. The many lives of active galactic nuclei: cooling flows, black holes and the luminosities and colours of galaxies. MNRAS, 365:11–28, 2006.

R. Davé, B. D. Oppenheimer, and S. Sivanandam. Enrichment and pre-heating in intragroup gas from galactic outflows. MNRAS, 391:110–123, 2008.

G. de Vaucouleurs. Recherches sur les Nebuleuses Extragalactiques. *Annales d'Astrophysique*, 11:247–+, 1948.

S. Diehl and T. S. Statler. The Hot Interstellar Medium of Normal Elliptical Galaxies. I. A Chandra Gas Gallery and Comparison of X-Ray and Optical Morphology. ApJ, 668:150–167, 2007.

S. Diehl and T. S. Statler. The Hot Interstellar Medium of Normal Elliptical Galaxies. II. Morphological Evidence for Active Galactic Nucleus Feedback. ApJ, 680:897–910, 2008a.

S. Diehl and T. S. Statler. The Hot Interstellar Medium in Normal Elliptical Galaxies. III. The Thermal Structure of the Gas. ApJ, 687:986–996, 2008b.

S. Djorgovski and M. Davis. Fundamental properties of elliptical galaxies. ApJ, 313:59–68, 1987.

A. Dressler, D. Lynden-Bell, D. Burstein, R. L. Davies, S. M. Faber, R. Terlevich, and G. Wegner. Spectroscopy and photometry of elliptical galaxies. I - A new distance estimator. ApJ, 313:42–58, 1987.

J. Dubinski. The Origin of the Brightest Cluster Galaxies. ApJ, 502:141–+, 1998.

S. C. Ellis and E. O'Sullivan. Correlations of near-infrared, optical and X-ray luminosity for early-type galaxies. MNRAS, 367:627–645, 2006.

G. Fabbiano, D.-W. Kim, and G. Trinchieri. An X-ray catalog and atlas of galaxies. ApJS, 80:531–644, 1992.

S. M. Faber, S. Tremaine, E. A. Ajhar, Y.-I. Byun, A. Dressler, K. Gebhardt, C. Grillmair, J. Kormendy, T. R. Lauer, and D. Richstone. The Centers of Early-Type Galaxies with HST. IV. Central Parameter Relations. AJ, 114: 1771–+, 1997.

A. C. Fabian. Cooling Flows in Clusters of Galaxies. ARA&A, 32:277–318, 1994.

A. C. Fabian, R. F. Mushotzky, P. E. J. Nulsen, and J. R. Peterson. On the soft X-ray spectrum of cooling flows. MNRAS, 321:L20–L24, 2001.

A. C. Fabian, S. W. Allen, C. S. Crawford, R. M. Johnstone, R. G. Morris, J. S. Sanders, and R. W. Schmidt. The missing soft X-ray luminosity in cluster cooling flows. MNRAS, 332:L50–L54, 2002.

A. C. Fabian, J. S. Sanders, G. B. Taylor, S. W. Allen, C. S. Crawford, R. M. Johnstone, and K. Iwasawa. A very deep Chandra observation of the Perseus cluster: shocks, ripples and conduction. MNRAS, 366:417–428, 2006.

W. Forman, C. Jones, and W. Tucker. Hot coronae around early-type galaxies. ApJ, 293:102–119, 1985.

Y. Fujita, J. Fukumoto, and K. Okoshi. Evolution of the Multiphase Hot Interstellar Medium in Elliptical Galaxies. ApJ, 488:585–+, October 1997. doi: 10.1086/304725.

Y. Fukazawa, J. G. Botoya-Nonesa, J. Pu, A. Ohto, and N. Kawano. Scaling Mass Profiles around Elliptical Galaxies Observed with Chandra and XMM-Newton. ApJ, 636:698–711, 2006.

M. Gaspari, C. Melioli, F. Brighenti, and A. D'Ercole. The dance of heating and cooling in galaxy clusters: three-dimensional simulations of self-regulated active galactic nuclei outflows. MNRAS, 411:349–372, 2011.

F. Gastaldello, D. A. Buote, P. J. Humphrey, L. Zappacosta, J. S. Bullock, F. Brighenti, and W. G. Mathews. Probing the Dark Matter and Gas

Fraction in Relaxed Galaxy Groups with X-Ray Observations from Chandra and XMM-Newton. ApJ, 669:158–183, 2007.

J. E. Gunn and J. R. Gott, III. On the Infall of Matter Into Clusters of Galaxies and Some Effects on Their Evolution. ApJ, 176:1–+, 1972.

F. Guo and W. G. Mathews. Simulating X-ray Supercavities and Their Impact on Galaxy Clusters. ApJ, 712:1311–1320, 2010a.

F. Guo and W. G. Mathews. Cosmic Ray-Dominated AGN Jets and the Formation of X-ray Cavities in Galaxy Clusters. *ArXiv e-prints*, 2010b.

S. F. Helsdon, T. J. Ponman, E. O'Sullivan, and D. A. Forbes. X-ray luminosities of galaxies in groups. MNRAS, 325:693–706, 2001.

M. Henriksen and S. Cousineau. An X-Ray Survey of Galaxies in Pairs. ApJ, 511:595–611, 1999.

P. J. Humphrey and D. A. Buote. A Chandra Survey of Early-Type Galaxies. I. Metal Enrichment in the Interstellar Medium. ApJ, 639:136–156, 2006.

P. J. Humphrey and D. A. Buote. The slope of the mass profile and the tilt of the Fundamental Plane in early-type galaxies. MNRAS, 403:2143–2151, 2010.

P. J. Humphrey, D. A. Buote, F. Gastaldello, L. Zappacosta, J. S. Bullock, F. Brighenti, and W. G. Mathews. A Chandra View of Dark Matter in Early-Type Galaxies. ApJ, 646:899–918, 2006.

J. Ji, J. A. Irwin, A. Athey, J. N. Bregman, and E. J. Lloyd-Davies. Elemental Abundances in the X-Ray Gas of Early-Type Galaxies with XMM-Newton and Chandra Observations. ApJ, 696:2252–2268, 2009.

R. Johnson, D. Chakrabarty, E. O'Sullivan, and S. Raychaudhury. Comparing X-ray and Dynamical Mass Profiles in the Early-type Galaxy NGC 4636. ApJ, 706:980–994, 2009.

C. Jones, W. Forman, A. Vikhlinin, M. Markevitch, L. David, A. Warmflash, S. Murray, and P. E. J. Nulsen. Chandra Observations of NGC 4636-an Elliptical Galaxy in Turmoil. ApJ, 567:L115–L118, 2002.

D. Kawata and B. K. Gibson. GCD+: a new chemodynamical approach to modelling supernovae and chemical enrichment in elliptical galaxies. MNRAS, 340:908–922, 2003.

D. Kawata and B. K. Gibson. Self-regulated active galactic nuclei heating in elliptical galaxies. MNRAS, 358:L16–L20, 2005.

C. C. Kirkpatrick, M. Gitti, K. W. Cavagnolo, B. R. McNamara, L. P. David, P. E. J. Nulsen, and M. W. Wise. Direct Evidence for Outflow of Metal-Enriched Gas Along the Radio Jets of Hydra A. ApJ, 707:L69–L72, 2009.

C. C. Kirkpatrick, B. R. McNamara, and K. W. Cavagnolo. Anisotropic Metal-enriched Outflows Driven by Active Galactic Nuclei in Clusters of Galaxies. ApJ, 731:L23+, 2011.

L. D. Landau and E. M. Lifshitz. *Fluid mechanics*. Pergamon Press, 1959.

E. J. Lloyd-Davies, T. J. Ponman, and D. B. Cannon. The entropy and energy of intergalactic gas in galaxy clusters. MNRAS, 315:689–702, 2000.

M. Loewenstein and W. G. Mathews. Hot gas metallicity and the history of supernova activity in elliptical galaxies. ApJ, 373:445–451, 1991.

M. Loewenstein, E. G. Zweibel, and M. C. Begelman. Cosmic-ray heating of cooling flows - A critical analysis. ApJ, 377:392–402, 1991.

C. L. Martin, H. A. Kobulnicky, and T. M. Heckman. The Metal Content of Dwarf Starburst Winds: Results from Chandra Observations of NGC 1569. ApJ, 574:663–692, 2002.

W. G. Mathews. On the global ecology of elliptical galaxies. AJ, 97:42–56, 1989.

W. G. Mathews. Interstellar events in elliptical galaxies. ApJ, 354:468–482, 1990.

W. G. Mathews and J. C. Baker. Galactic Winds. ApJ, 170:241–+, 1971.

W. G. Mathews and F. Brighenti. Hot Gas in and around Elliptical Galaxies. ARA&A, 41:191–239, 2003a.

W. G. Mathews and F. Brighenti. Rapid Cooling of Dusty Gas in Elliptical Galaxies. ApJ, 590:L5–L8, 2003b.

W. G. Mathews and F. Brighenti. Creation of the X-Ray Cavity Jet and Its Radio Lobe in M87/Virgo with Cosmic Rays: Relevance to Relic Radio Sources. ApJ, 676:880–888, 2008.

W. G. Mathews, F. Brighenti, and D. A. Buote. Time-dependent Circulation Flows: Iron Enrichment in Cooling Flows with Heated Return Flows. ApJ, 615:662–674, 2004.

W. G. Mathews, A. Faltenbacher, F. Brighenti, and D. A. Buote. Baryonically Closed Galaxy Groups. ApJ, 634:L137–L140, 2005.

W. G. Mathews, F. Brighenti, A. Faltenbacher, D. A. Buote, P. J. Humphrey, F. Gastaldello, and L. Zappacosta. Large Scatter in X-Ray Emission among Elliptical Galaxies: Correlations with Mass of Host Halo. ApJ, 652:L17–L20, 2006.

B. R. McNamara and P. E. J. Nulsen. Heating Hot Atmospheres with Active Galactic Nuclei. ARA&A, 45:117–175, 2007.

Y. Mellier and G. Mathez. Deprojection of the de Vaucouleurs R exp 1/4 brightness profile. A&A, 175:1–3, 1987.

D. Merritt. Relaxation and tidal stripping in rich clusters of galaxies. III - Growth of a massive central galaxy. ApJ, 289:18–32, 1985.

D. Merritt and L. Ferrarese. The $M_{\bullet}$-σ Relation for Supermassive Black Holes. ApJ, 547:140–145, 2001.

J. S. Mulchaey and T. E. Jeltema. Hot Gas Halos in Early-type Field Galaxies. ApJ, 715:L1–L5, 2010.

J. F. Navarro, C. S. Frenk, and S. D. M. White. The Structure of Cold Dark Matter Halos. ApJ, 462:563–+, 1996.

H. Omma, J. Binney, G. Bryan, and A. Slyz. Heating cooling flows with jets. MNRAS, 348:1105–1119, 2004.

J. P. F. Osmond and T. J. Ponman. The GEMS project: X-ray analysis and statistical properties of the group sample. MNRAS, 350:1511–1535, 2004.

E. O'Sullivan, D. A. Forbes, and T. J. Ponman. A catalogue and analysis of X-ray luminosities of early-type galaxies. MNRAS, 328:461–484, 2001.

E. O'Sullivan, J. M. Vrtilek, A. M. Read, L. P. David, and T. J. Ponman. An XMM-Newton observation of the galaxy group MKW 4. MNRAS, 346: 525–539, 2003.

E. O'Sullivan, J. M. Vrtilek, and J. C. Kempner. Active Galactic Nucleus Feedback and Gas Mixing in the Core of NGC 4636. ApJ, 624:L77–L80, 2005.

J. R. Peterson and A. C. Fabian. X-ray spectroscopy of cooling clusters. Phys. Rep., 427:1–39, 2006.

J. R. Peterson, F. B. S. Paerels, J. S. Kaastra, M. Arnaud, T. H. Reiprich, A. C. Fabian, R. F. Mushotzky, J. G. Jernigan, and I. Sakelliou. X-ray imaging-spectroscopy of Abell 1835. A&A, 365:L104–L109, 2001.

E. C. D. Pope. Observable consequences of kinetic and thermal AGN feedback in elliptical galaxies and galaxy clusters. MNRAS, 395:2317–2325, 2009.

E. C. D. Pope, A. Babul, G. Pavlovski, R. G. Bower, and A. Dotter. Mass transport by buoyant bubbles in galaxy clusters. MNRAS, 406:2023–2037, 2010.

A. E. Sansom, E. O'Sullivan, D. A. Forbes, R. N. Proctor, and D. S. Davis. X-ray observations of three young, early-type galaxies. MNRAS, 370:1541–1555, 2006.

C. L. Sarazin. X-ray emission from clusters of galaxies. *Reviews of Modern Physics*, 58:1–115, 1986.

C. L. Sarazin, J. A. Irwin, and J. N. Bregman. Chandra X-Ray Observations of the X-Ray Faint Elliptical Galaxy NGC 4697. ApJ, 556:533–555, 2001.

A. Sternberg and N. Soker. Sound waves excitation by jet-inflated bubbles in clusters of galaxies. MNRAS, 395:228–233, 2009.

J. M. Stone and M. L. Norman. ZEUS-2D: A radiation magnetohydrodynamics code for astrophysical flows in two space dimensions. I - The hydrodynamic algorithms and tests. ApJS, 80:753–790, 1992.

R. S. Sutherland and M. A. Dopita. Cooling functions for low-density astrophysical plasmas. ApJS, 88:253–327, 1993.

G. Tabor and J. Binney. Elliptical Galaxy Cooling Flows Without Mass Drop-Out. MNRAS, 263:323–+, 1993.

P. Temi, F. Brighenti, and W. G. Mathews. Far-Infrared Spitzer Observations of Elliptical Galaxies: Evidence for Extended Diffuse Dust. ApJ, 660:1215–1231, 2007a.

P. Temi, F. Brighenti, and W. G. Mathews. Spitzer Observations of Transient, Extended Dust in Two Elliptical Galaxies: New Evidence of Recent Feedback Energy Release in Galactic Cores. ApJ, 666:222–230, 2007b.

P. A. Thomas. A cooling flow in the giant, elliptical galaxy NGC 4472. MNRAS, 220:949–969, 1986.

T. Toniazzo and S. Schindler. Gas dynamic stripping and X-ray emission of cluster elliptical galaxies. MNRAS, 325:509–530, 2001.

L. Tornatore, S. Borgani, V. Springel, F. Matteucci, N. Menci, and G. Murante. Cooling and heating the intracluster medium in hydrodynamical simulations. MNRAS, 342:1025–1040, 2003.

W. H. Tucker and R. Rosner. Thermal conduction and heating by nonthermal electrons in the X-ray halo of M87. ApJ, 267:547–550, 1983.

G. M. Voit and M. Donahue. Problems with Cold Clouds and Cooling Flows. ApJ, 452:164–+, October 1995. doi: 10.1086/176288.

R. Weaver, R. McCray, J. Castor, P. Shapiro, and R. Moore. Interstellar bubbles. II - Structure and evolution. ApJ, 218:377–395, 1977.

R. E. White, III and C. L. Sarazin. Star formation in X-ray cluster cooling flows. ApJ, 318:612–620, 1987.

R. E. White, III and C. L. Sarazin. Evidence for environmental effects on early-type galaxy X-ray halos. ApJ, 367:476–489, 1991.

H. Xu, S. M. Kahn, J. R. Peterson, E. Behar, F. B. S. Paerels, R. F. Mushotzky, J. G. Jernigan, A. C. Brinkman, and K. Makishima. High-Resolution Observations of the Elliptical Galaxy NGC 4636 with the Reflection Grating Spectrometer on Board XMM-Newton. ApJ, 579:600–606, 2002.